From polysilazanes to highly micro-/mesoporous Si3N4 containing in situ immobilized Co or Ni-based nanoparticles

Maíra Mallmann, Rafael Nishihora, Emanoelle Diz Acosta, Pierre Carles, Norifumi Asakuma, Shotaro Tada, Yuji Iwamoto, Umit Demirci, Ricardo Machado, Samuel Bernard

From polysilazanes to highly micro-/mesoporous Si_3N_4 containing *in situ* immobilized Co or Ni-based nanoparticles

Maíra Mallmann[a,b], Rafael Nishihora[a,b], Emanoelle Diz Acosta[b], Pierre Carles[a], Norifumi Asakuma[c], Shotaro Tada[c], Yuji Iwamoto[c], Umit Demirci[d], Ricardo Machado[b], Samuel Bernard[a]*

[a] Univ. de Limoges, CNRS, IRCER, UMR 7315, F-87000, Limoges, France

[b] Department of Chemical Engineering, Federal University of Santa Catarina, 88010-970 Florianopolis, Brazil

[c] Department of Materials Science and Engineering, Graduate School of Engineering, Nagoya Institute of Technology, Showa-ku, Nagoya 466-8555, Japan

[d] Institut Européen des Membranes, IEM – UMR 5635, ENSCM, CNRS, Université de Montpellier, Montpellier

* Corresponding author: Université de Limoges, CNRS, IRCER, UMR 7315, F-87000, Limoges, France

E-mail address: samuel.bernard@unilim.fr (S. Bernard)

Abstract

The *in-situ* immobilization of cobalt (Co) or nickel (Ni) nanoparticles (NPs) in highly micro-/mesoporous polymer-derived silicon nitride (Si_3N_4) has been achieved. It is accomplished by the coordination of a polysilazane with metal chlorides ($CoCl_2$ or $NiCl_2$) followed by the subsequent pyrolysis of the metal:organosilicon polymer coordination complex in the temperature range 700 - 1000 °C in flowing ammonia. By coupling X-ray diffraction (XRD) and high-resolution transmission electron microscopy (HR-TEM), it has been shown that the phase composition and crystallinity as well as the crystal size of

the metal particles are controlled by tuning the synthesis conditions including the Si:metal ratio, the reaction time and the type of polysilazane as well as the heat-treatment temperature. This has been discussed in details. Then, to exploit the catalytic activity of metal NPs towards the hydrolysis of sodium borohydride ($NaBH_4$), we have developed the micro-/mesoporosity of the Si_3N_4 matrix using a nano-casting approach. Hence, materials with BET specific surface areas (SSA) as high as 921.5 $m^2.g^{-1}$ have been delivered to measure their potential for catalysis.

Keywords

Polysilazane; specific surface area; non noble transition metals

1. Introduction

Clean and sustainable energy technologies such as water splitting, CO_2 reduction, N_2 fixation, H_2 fuel cell production or catalytic abatement of major pollutants in air such as NO_x, Volatile Organic Compounds (VOCs) and CO are currently under intensive research and development because of their high efficiency, promising large-scale applications in the future and can be utilized with virtually no pollution or greenhouse gas emissions [1–4].

Catalysis is highly relevant for the development of clean and sustainable energy technologies. However, most of these energy technologies use noble metal catalysts (*e.g.*, platinum, Pt, and the derivative Pt group metals (PGM)) to promote key chemical reactions [5–7]. PGM show outstanding catalytic activities and durability under various pH conditions but their limited availabilityand high-cost hamper large-scale applications. The development of low cost, earth-abundant and highly efficient alternatives to PGM

via materials discovery as a key element for adoption of clean and sustainable energy technologies is essential [5].

On the one hand, the expected high activity of non-noble transition metals (TM) such as Co and Ni along with their attractive cost compared with that of noble metal catalysts has sparked a growing interest in the synthesis of such metals as nanoparticles (NPs). These materials are particularly relevant for use in alkaline media environments (because their active oxide counterparts are stable in such an environment) to meet the requirements of high activity, selectivity and long-term stability with superiority to competitors (*e.g.* PGM) [6–8].

On the other hand, advanced ceramics are high value-added products for clean and sustainable energy technologies; especially when used as durable supports on which the catalyst – the metal - is deposited in form of NPs [9,10]. However, aggregation and sintering of NPs usually cause loss of catalytic performance. Immobilization of catalytically active metal NPs on/within a high-surface-area inorganic support may partially alleviate this deficiency [11].

Based on these preconceptions, a very convenient precursor route - the polymer derived ceramics (PDCs) route - allows the formation of the support and the catalysts in an one-step process; thus, the issues related to particle agglomeration and removal from the support are avoided. This approach has been recently utilized for the preparation of metal/Si-based (oxy-)carbide and carbonitride compounds such as Ni/SiC [12], Ni/SiOC [13], Ni/SiCN(O) [14] and M/SiCN (M = Pd and Ru [15], Pd_2Ru [16], Cu [17,18] , Ir [19], Ni [20], Pt [21], Co [22], Fe [23]) derived from metal-modified polycarbosilanes, polysiloxanes and polysilazanes, respectively. Likewise, the effects of TM on the evolution of polymer-derived SiOC have been investigated [24,25]. Also, Co/Ni–SiOC materials have been tested as electrocatalysts for the oxygen reduction reaction (ORR)

[26]. In contrast, the one-step immobilization of TM NPs in a Si_3N_4 matrix systems (*i.e.*, TM/Si_3N_4) for heterogeneous catalysis has never been demonstrated. These components may be particularly attractive as supports and catalysts themselves [27–32].

Very recently, the *in-situ* formation of Co [33] and Ni [34] in Si_3N_4 at a temperature as low as 400 °C using perhydropolysilazane (PHPS) as a Si_3N_4 precursor and ammonia [33] or nitrogen [34] as a pyrolysis atmosphere has been reported. Herein, the preparation of highly micro-/mesoporous Si_3N_4-encapsulated Co or Ni NPs with various TM contents through a coupling approach based on the PDCs route and a nano-casting strategy is achieved (Fig. 1).

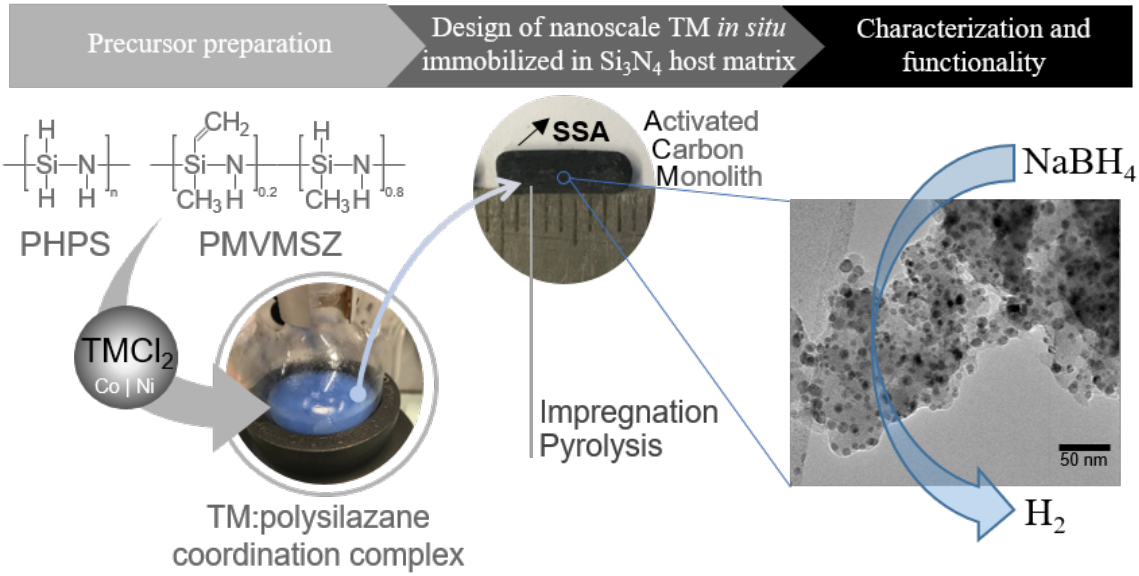

Fig. 1. Flow diagram of the general process of designing micro-/mesoporous TM (TM = Co, Ni)/Si_3N_4 nanocomposites from polysilazanes.

The preparation has been conducted based on the preparation of a set of Co- or Ni-containing polysilazanes (Fig. 1) in the temperature range 700 – 1000 °C and as-obtained compounds have been characterized in details. They have been investigated as self-supported nanocatalysts for the hydrolysis of alkaline aqueous sodium borohydride [35], [36]. While this does not identify the most efficient material for H_2 release from $NaBH_4$

it establishes a route to the development of a novel generation of durable self-supported nanocatalysts via a simple method using inexpensive precursors.

2. Experimental

2.1 Materials

The synthesis of the precursors is carried out in a purified argon atmosphere passing through a column of phosphorus pentoxide and then through a Schlenk line. The cleaned glassware is stored in an oven at 95 °C overnight before being connected to the Schlenk line, assembled, and pumped under reduced pressure for 30 min and then filled with argon. All chemical products are handled in an argon-filled glove box (Jacomex, Campus-type; O_2 and H_2O concentrations kept at ≤0.1 ppm and ≤0.8 ppm, respectively). Perhydropolysilazane labelled PHPS in a 20 vol% concentration in di-n-buthylether (commercial name: NN120-20) and poly(methylvinyl-*co*-methyl)silazane labeled PMVMSZ (commercial name: Durazane® 1800) were provided by durXtreme GmbH, Germany, stored in a freezer and used as-received. Anal. Found (wt%): Si, 67.2; C, 2.2; N, 24.0; H, 6.2; O, 0.4. $[Si_{1.0}C_{0.1}N_{0.7}O_{0.0}H_{2.6}]_n$ (*Normalized to total 100 wt % (total of wt% was 99.5 wt%) and reference to* $Si_{1.0.}$ *Oxygen content (below 2 wt%) omitted in the empirical formulae*). FTIR (ATR/cm^{-1}): ν(N−H) = 3377 (m), ν(Si−H) = 2141 (vs), δ(N-H): 1167 (m), δ(N−Si−N) = 812 (vs). ^{1}H NMR (300 MHz, C_6D_6, δ/ppm): 1.6-0.3 (br, N*H*), 5.8-4.3 (br, Si*H*). The Durazane® 1800 labelled here PMVMSZ was provided by Merck Company, Germany, stored in a fridge and used as-received. Anal. found (wt%): Si, 41.3; C, 27.3; N, 22.7; H, 8.3; O, 0.4. $[Si_{1.0}C_{1.5}N_{1.1}H_{5.5}]_n$ (*Normalized to total 100 wt % (total of wt% was 98.9 wt%) and reference to* $Si_{1.0.}$ *Oxygen content (below 2 wt%) omitted in the empirical formulae*). FTIR (ATR/cm^{-1}): ν(N−H) = 3381 (s), ν(C−H in vinyl) = 3058 (m), ν(C−H in methyl) = 2954 (s), 2902 (m) and 2848 (w), ν(Si−H) = 2123

(s), δ(C=C) = 1594 (w), δ(=C-H) = 1405 (w), δ(Si−CH_3) = 1251 (m), δ(N-H): 1169 (s), δ(C=C/=CH_2) = 947 (w), ν(N−Si−N) = 897 (vs), δ(Si-CH_3) = 787 (m); ^{1}H NMR (300 MHz, $CDCl_3$, δ/ppm): 0.4–0.1 (br, $SiCH_3$), 1.1–0.5 (br, NH), 4.9–4.4 (br, SiH), 6.3–5.7 (br, vinyl). Toluene (99.85%, Extra Dry over Molecular Sieve, AcroSeal(R)) was purchased from Acros Organics™. The metal chlorides, nickel(II) chloride 98 % and cobalt(II) chloride, anhydrous for synthesis, were obtained from Sigma-Aldrich and Merck KGaA, respectively. Activated carbon monoliths labelled as AC were of type NORIT RX3 (Cabot Corporation) with a purity of 97 % (SSA = 989 $m^2.g^{-1}$; Vp = 0.51 $cm^3.g^{-1}$; Øp = 4.3 nm).

2.2 Preparation of the precursors

The precursor preparation consisted to add under argon a solution of polysilazane (PHPS or PMVMSZ) in toluene (thus di-n-buthylether is first extracted from PHPS) to a suspension of previously weighed (in the glove-box) $CoCl_2$ or $NiCl_2$ in toluene in a three-necked round-bottomed flask and to proceed to the heating of the mixture at toluene reflux. In a typical experiment, 3 g of PHPS (66 mmol) (referred to the theoretical monomeric unit of the polymer) are quickly added with a syringe under flowing argon to a solution of 50 mL of toluene with 1.72 g of $CoCl_2$ (13.25 mmol) at RT under vigorous stirring. Then, the temperature is increased up to toluene reflux under static argon and kept at this temperature under vigorous stirring for 72 h. After cooling down, the solvent is extracted via an ether bridge (40 °C/1.5.10^{-1} mbar) to release an air- and moisture-sensitive Co-modified PHPS labelled **PHCo5-72** (*5* being the Si:Co ratio) that appears as a blue solid polymer. Anal. found (wt %): Si 39.3, C 2.2, N 16.2, O 2.9, H 3.7, Co 16.7, Cl 19.8. $[Si_{1.0}C_{0.1}N_{0.8}O_{0.1}H_{2.6}Co_{0.2}Cl_{0.4}]_n$ (*Normalized to total 100 wt % (total of wt% was 99.2 wt%) and reference to* $Si_{1.0.}$ *Oxygen content (below 2 wt%) omitted in the empirical*

formulae). FTIR (ATR/cm^{-1}): ν(N−H) = 3375 (w), ν(Si−H) = 2161 (s), ν(Co−Cl) = 1620 (s), 1400 (w), δ(N-H): 1182 (m), 1016 (w), δ(N−Si−N) = 835 (vs).

Six samples have been prepared according to this procedure by changing:

i. The Si:Co ratio from 2.5 to 25 using PHPS as a pre-formed polymer and a time of reaction at toluene reflux overnight. Samples are labelled **PHCo2.5**, **PHCo5**, **PHCo25**;

ii. The type of TM (Co and Ni) using PHPS as a pre-formed polymer and fixing a Si:TM ratio of 5 and a time of reaction at toluene reflux of 72 h. The samples are labelled **PHCo5-72** and **PHNi5-72**;

iii. The type of the preformed polymer using PMVMSZ and fixing a Si:Co ratio of 5 and a time of reaction at toluene reflux of 72 h. The sample is labelled **PMCo5-72**;

2.3 Heat-treatment of precursors

Polymer samples are then placed in alumina boats in the glovebox, introduced in a sealed tube under argon atmosphere to prevent any oxygen contamination of the samples during the following transfer into a silica tube inserted in a horizontal furnace (Carbolite BGHA12/450B) under argon. The tube is evacuated (0.1 mbar) and refilled with ammonia (99.995 %) to atmospheric pressure. Subsequently, the samples are subjected to a cycle of ramping of 5 °C.min^{-1} in the temperature range RT–1000 °C in flowing ammonia (dwelling time of 2 h at the temperature selected among 700, 800, 900 and 1000 °C). A constant flow (120 mL.min^{-1}) is passed through the tube during the pyrolysis cycle. After cooling under argon atmosphere, as-pyrolyzed samples are stored in the glovebox for characterization. Samples are labelled by adding '_T' to the name of the precursors with T being the first (if T < 1000 °C) or two first (if T = 1000 °C) digits of the temperature at

which the precursors have been exposed. For example, the **PHCo5_10** sample represents the **PHCo5** sample heat-treated at 1000 °C.

2.4 Design of micro-/mesoporous monoliths

The precursors have been used to coat AC samples. The latter is previously heat-treated at 600 °C under reduced pressure (3.10^{-1} mbar) for 10 hours to remove the presence of any trace of oxygen, moisture, or dangling groups (-OH, -COOH, etc.) without structure modification; then, they have been stored inside the glove box. A specific weight of AC is taken from the glove box in a Schlenk-type flask to be put under reduced pressure before deposition of the polymeric samples in solution (5 wt%). AC samples are infiltrated at reduced pressure according to an optimum mass ratio between the polymer and AC (1.4) [12], [37]. Then, the composites are allowed to age for 24 h under static vacuum with continuous ultra-sonication. After aging for 24 h, a filtration step is performed, and the composites are washed with toluene under argon flow. Excess of liquid is removed using a syringe and then the solvent is evaporated at low pressure (5.10^{-1} mbar) at 30 °C for 2 h to generate the coated AC. The impregnated monoliths are dried and transferred under protective atmosphere into a horizontal tube furnace (Thermoconcept® OS50/450/12) to be subjected to a cycle of ramping at 100 °C.h^{-1} to 400 °C under nitrogen, dwelling there for 2 h. This is followed by a pyrolysis under ammonia at 100 °C.h^{-1} at the final temperature fixed in the range 700 – 1000 °C, dwelling there for 2 h. Cooling to RT at 120 °C.h^{-1} produced the porous samples labelled by adding 'm' to the name of the ceramic product. For example, the **mPHCo5_10** sample represents the mesoporous sample produced from **PHCo5** by heat-treatment at 1000 °C.

2.5 Characterization

The chemical structure of polymers has been determined by transmission FTIR spectroscopy using a Nicolet 6700 Thermofisher equipment working from 4000 to 400 cm^{-1}. The data are collected by Omnic™ Software. Chemical analyses of the polymers have been performed at Mikroanalytisches Labor Pascher (Remagen, Germany). TG analyses have been carried out in flowing nitrogen at 5 °C.min^{-1} to 1000 °C using alumina crucibles at ambient atmospheric pressure (STA 449 F3, Netzsch GmbH, Selb, Germany). As-obtained ceramic samples isolated at different pyrolysis temperatures are crushed into fine powders and evenly spread on Si low background sample holders (Bruker™). Then, their phase composition is determined by XRD analysis (Bruker AXS D8 Discover, CuK_α radiation, Billerica, Massachussets, USA). As-obtained XRD patterns hav been compared to reference patterns of the Powder Diffraction File of the International Centre for Diffraction Data (ICDD; PDF-4+: fcc-Co: 00-015-0806, hcp-Co: 04-001-3273, CoSi: 01-079-8014, Co_2Si: 04-003-2126, Co_2SiO_4: 01-070-2115, fcc-Ni: 00-004-0850, α-Si_3N_4: 04-005-5074 and β-Si_3N_4: 04-033-1160). The produced ceramic monoliths have been characterized by nitrogen gas adsorption-desorption measurements at 77 K. The Brunauer–Emmett–Teller (BET) method has been used to calculate the specific surface area of the samples. The modal pore diameter (MPD) is derived from the desorption branches of the isotherms using the *Barrett–Joyner–Halenda* (BJH) method whereas the total pore volume is estimated from the amount of N_2 adsorbed at a relative pressure (P/P_0) of 0.97. The data are collected using a 3Flex Physisorption equipment, from Micrometrics Instrument Corporation. The chemical analysis of selected powders has been done by scanning electron microscopy equipped with energy dispersive spectroscope (EDS-SEM, JEOL IT 300 LV, Tokyo, Japan). The samples are positioned on metallic stubs with the aid of a water-based conductive graphene carbon paint. A drop of liquid, colloidal silver is placed in the side of the sample to increase conductivity. Structural and morphological

characterizations have been conducted on powders by Transmission Electron Microscopy with a JEM-2100F model from JEOL (Japan) for **PHCo5-72_8**, **PHCo5-72_10**, **PMCo5-72_10** and **PHNi5-72_10** samples. The hydrolysis of $NaBH_4$ has been performed at 80 °C in a highly alkaline medium (pH > 10). In a typical experiment, 16 mg of the porous samples are introduced in 1 mL solution of $NaBH_4$ (120 mg in 2 % NaOH) into a reactor (glass tube) that is sealed with a silicon septum and Parafilm®, and connected to a water-filled inverted burette (water coloured in blue) via a cold trap for steam, maintained at 0 °C. Then, the reactor is immersed in an oil bath kept at 80 °C. A camera records the water displacement in the inverted burette due to hydrogen generation. Hydrogen starts to evolve rapidly, and the evolution is video recorded for 180 min, to be then computationally analysed post-hydrolysis.

3. Results and discussion

3.1 Precursor preparation

Our general approach consists in the addition of a solution of polysilazane (PHPS or PMVMSZ) in toluene to a suspension of nickel or cobalt chloride ($NiCl_2$ or $CoCl_2$) in toluene at room temperature (RT). Then, the temperature is gradually increased to toluene reflux, keeping the mixture for 72 h before cooling down and extracting the solvent. A controlled molar (or atomic) ratio between metal chloride (TM) and the considered polysilazane (Si) is applied. Following this strategy, we have synthesized a first series of three representative polymers with a Si:TM (TM = Co or Ni) ratio of 5 by changing (1) the type of pre-formed polymer (PH for PHPS or PM for PMVMSZ) and (2) the nature of TM (Co or Ni). These three samples are labelled as **PHCo5-72**, **PHNi5-72** and **PMCo5-72**. There is an additional series for which the Si:TM (TM = Co) ratio has been changed from 2.5 to 25 according to the quantity of $CoCl_2$ added to the solution of PHPS.

The dwelling time at toluene reflux has been maintained overnight. Such polymers are denoted **PHCo2.5**, **PHCo5** and **PHCo25**.

PHPS or PMVMSZ do not exhibit the same reactivity towards TM chlorides (TM = Co, Ni): after solvent extraction, all the samples derived from PHPS are solid and insoluble compounds whereas **PMCo5-72** (derived from PMVMSZ) remains liquid with a higher viscosity than PMVMSZ (Fig. 2). This is discussed hereafter.

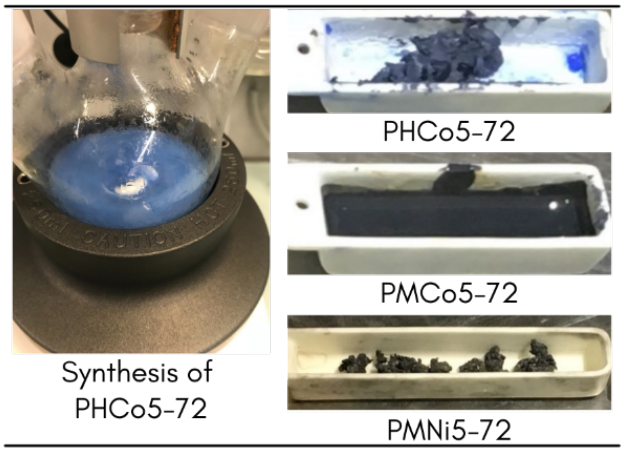

Fig. 2. Illustrations of the synthesis of TM-modified polysilazanes and polymers after solvent extraction.

The samples have been thoroughly investigated by FTIR spectroscopy (Fig. 3 and Fig. S1 (Supplementary Material)) whereas the **PHCo5-72** sample has been further selected and characterized by elemental analysis (Table 1). As reference samples, the FTIR spectra of PHPS and PMVMSZ and their elemental composition has been analyzed. As displayed in Fig. 3, the ATR-FTIR spectrum of PHPS shows the bands associated with νN–H (3377 cm^{-1}), νSi–H (2141 cm^{-1}), δNH of Si–NH–Si (1167 cm^{-1}) and δSi-N-Si (812 cm^{-1}). The ATR-FTIR spectrum of PMVMSZ shows the expected absorptions of polysilazanes through the bands attributed to –Si–NH–Si– groups such as N–H stretching at 3381 cm^{-1} and the vibration of the NH unit bridging two silicon atoms at 1169 cm^{-1}. It also highlights the typical bands of i) vinyl silyl groups (CH_2=CH–Si–) as C–H vibrations

at 3056 cm^{-1}, C=C stretching at 1594 cm^{-1}, and scissoring of terminal methylene at 1405 cm^{-1}, ii) Si-methyl groups with two bands located at 2954, 2902 and 2848 cm^{-1} and assigned to the C–H stretching and at 1251 cm^{-1} ($\delta(Si{-}CH_3)$) and iii) Si-H groups through the strong absorption band at 2123 cm^{-1}. The large bands in the 1000-500 cm^{-1} range can be attributed to C=C/=CH_2 groups at 947 cm^{-1}, Si-N stretching in Si-N-Si units centred at 897 cm^{-1} and Si-C bond stretching at 787 cm^{-1} most probably overlapping the deformation of Si-H units.

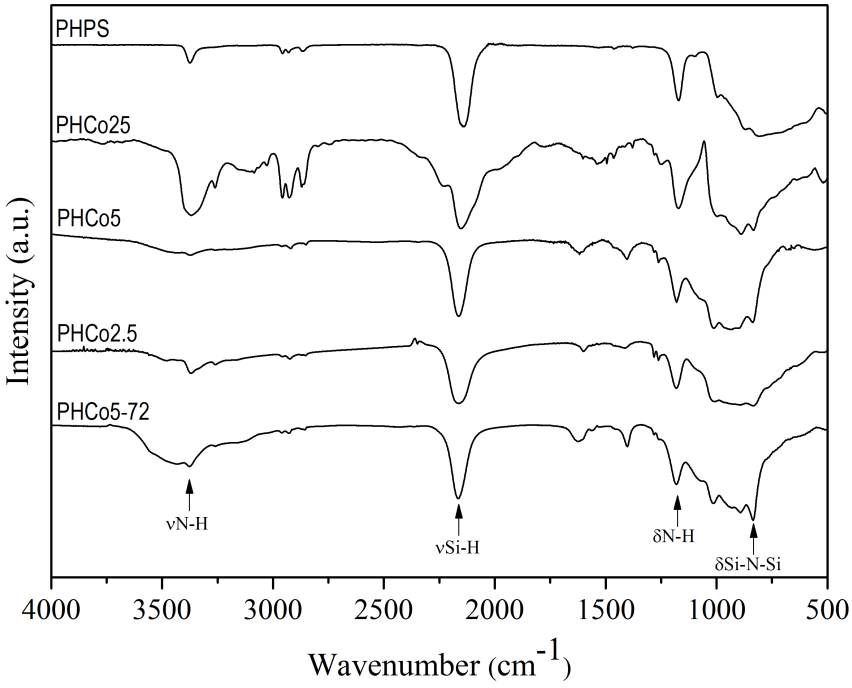

Fig. 3. FTIR spectra of PHPS, **PHCo25**, **PHCo5**, **PHCo2.5** and **PHCo5-72**.

Although the TM-modified polysilazanes show similar spectra (except **PHCo25** that still reports toluene signature because of an incomplete extraction), minor changes are identified, as previously reported [33]: the relative intensity of δN-H at 1167 cm^{-1} to νSi-N-Si at 812 cm^{-1} ($A_{N\text{-}H}/A_{Si\text{-}N\text{-}Si}$) in PHPS decreases with both the decrease of the Si:TM atomic ratio; thus with the increase of the TM content in all the samples (Fig. 3) and the duration of the reaction. This is evident by comparing the intensity ratios in the spectra of **PHCo5**, **PHCo2.5** and **PHCo5-72**. The spectrum of **PHCo5** displays an intensity ratio

of 0.72 (0.84 for PHPS) while the spectra of **PHCo2.5** and **PHCo5-72** exhibit intensity ratios of 0.67 and 0.62, respectively. This indicates a lower portion of N-H bonds in **PHCo2.5** and **PHCo5-72**. This tendency is also clear by comparing the relative intensity of νSi-H at 2141 cm^{-1} to νSi-N-Si ($A_{Si-H}/A_{Si-N-Si}$) in PHPS: it decreases after addition of $CoCl_2$ (by comparing the spectra of PHPS and Co-modified PHPS) which indicates that Si-H bonds are also affected by $CoCl_2$ addition. In addition, it evolves with the change of the Si:Co ratio from 5 (**PHCo5**) to 2.5 (**PHCo2.5**). The duration time at toluene reflux (overnight or 72 h) also affects this ratio by comparing the intensity ratios in the spectra of **PHCo5** and **PHCo5-72**: the former displays an intensity ratio of 1.0 (1.35 for PHPS) while the latter exhibits an intensity ratio of 0.82 indicating a lower portion of Si-H bonds in **PHCo5-72**. Interesting, the characteristic bands at 812 cm^{-1} (νSi-N-Si), at 1167 cm^{-1} (δN–H) and at 2143 cm^{-1} (νSi-H) in the spectrum of PHPS shift toward higher wavenumbers in Co-modified PHPS (respectively from 812 to 835 cm^{-1}, from 1167 to 1182 (**PHCo2.5**) cm^{-1} and from 2141 to 2167 (**PHCo2.5**) cm^{-1}) which is attributed to the highest degree of crosslinking of the delivered precursor. A hypothesis is that dehydrocoupling reactions between Si-H bonds together or between Si-H bonds and N-H bonds and/or transamination reactions [35–38] occur in our system by considering that TM compounds are well known to catalytically activate some of these reactions in the temperature range of 20 – 90 °C [35,38]. Therefore, Co-modified PHPS are expected to display a higher degree of crosslinking than PHPS. In this polymer system, both **PHCo2.5** and **PHCo5-72** samples would exhibit the highest degree of crosslinking because of the major occurrence of dehydrocoupling reaction and/or transamination reactions. Similar observations can be made in Fig. S1A (Supplementary Material) by changing Co into Ni (FTIR spectrum of **PHNi5-72**) regarding N-H bonds, but this does not affect the Si-H bonds. Thus, this indicates that Ni is well suited to catalyze transamination reactions –

involving N-H bonds - in our systems but it has a poor effect on dehydrocoupling. The tendency observed with Co-modified PHPS is not reflected in the FTIR spectrum of samples based on PMVMSZ used as a preformed polymer (FTIR spectrum of **PMCo5-72**) as shown in Fig. S1B (Supplementary Material). In the FTIR spectrum of **PMCo5-72**, the band at 3049 cm^{-1} is still present, which is assigned to the vibration of C–H bond in the vinyl groups. In addition, the typical absorption band arising from the stretching of C=C double bonds in vinyl groups is present at 1590 cm^{-1}. However, TM are also well known to catalytically activate hydrosilylation reactions [39–42], especially in our conditions (toluene reflux) [43,44]. Hence, it can be suggested that the higher steric hindrance imposed by the structure of PMVMSZ as well as the lowest concentration of reactive groups significantly limit the progress of the cross-linking reactions. This is highly reflected in the physical state of the samples.

According to the elemental analysis data of **PHCo5-72** provided in Table 1, the Si:TM ratio, fixed during the reagents mixing, is confirmed by measurements and they highlight the FTIR discussions. First, the elemental analysis data of **PHCo5-72** allows the determination of an empirical formula of $Si_{1.0}C_{0.1}N_{0.9}O_{0.1}H_{2.5}Co_{0.2}Cl_{0.4}$ (referenced to $Si_{1.0}$) to be compared to PHPS ($Si_{1.0}C_{0.1}N_{0.7}O_{0.0}H_{2.6}$). Because the atomic Cl:Co ratio calculated in **PHCo5-72** is equal to that one found in $CoCl_2$ and that the measured Si:Co ratio is 5, we suggest that no significant release of Cl and Si-containing species occurs during the synthesis, and that no reaction occurs between PHPS and $CoCl_2$.

Table 1

Elemental composition of PHPS and **PHCo5-72**.

Sample	Element content [wt%]							Chemical formula
	C	H	N	O	Co	Si	Cl	

PHPS	2.2	6.2	24.0	0.4	-	67.2	-	$Si_{1.0}C_{0.1}N_{0.7}O_{0.0}H_{2.6}$
PHCo5-72	2.2 ±0.03	3.6 ±0.03	16.7 ±0.4	2.5 ±0.02	16.5 ±0.05	38.9	19.6	$Si_{1.0}C_{0.1}N_{0.9}O_{0.1}H_{2.5}Co_{0.2}Cl_{0.4}$

In a first approximation, we suggest that a blended compound with the appropriate Si:Co ratio (=5) is delivered. However, the (slight) decrease of the Si:N ratio content in **PHCo5-72** compared to PHPS tends to confirm the formation of Si-N bonds in **PHCo5-72** which inherently results from dehydrocoupling reactions. Thus, TM (= Co, Ni)-modified PHPS most probably represents polysilazanes coordinated by TM (= Co, Ni) chlorides via silylamino groups in which dehydrocoupling reactions occur to further crosslink the PHPS network.

3.2 In-situ growth of nanoscale TM in the temperature range 700 to 1000 °C

Hereafter, identification of the crystalline phase composition in the samples formed by pyrolysis of precursors characterized previously from 700 to 1000 °C in flowing ammonia has been explored. The temperature 700 °C has been selected as the minimum temperature at which preceramic polymers is converted into ceramics [45]. 1000 °C is the temperature at which the sample is considered as sufficiently stable to be explored for further investigation in alkaline media. In addition, the analysis of XRD patterns has been investigated to reach the crystallite size evolution upon heat-treatment. Then, micro- and nanostructural information of selected samples have been collected by HR (High Resolution)-TEM.

Fig. 4 reports the XRD evolution of the samples labelled PHCoX_Y with X being the Si:Co ratio and Y the first digit of the pyrolysis temperature: **PHCo25_7**, **PHCo5_7**, **PHCo2.5_7** and **PHCo5-72_7** samples.

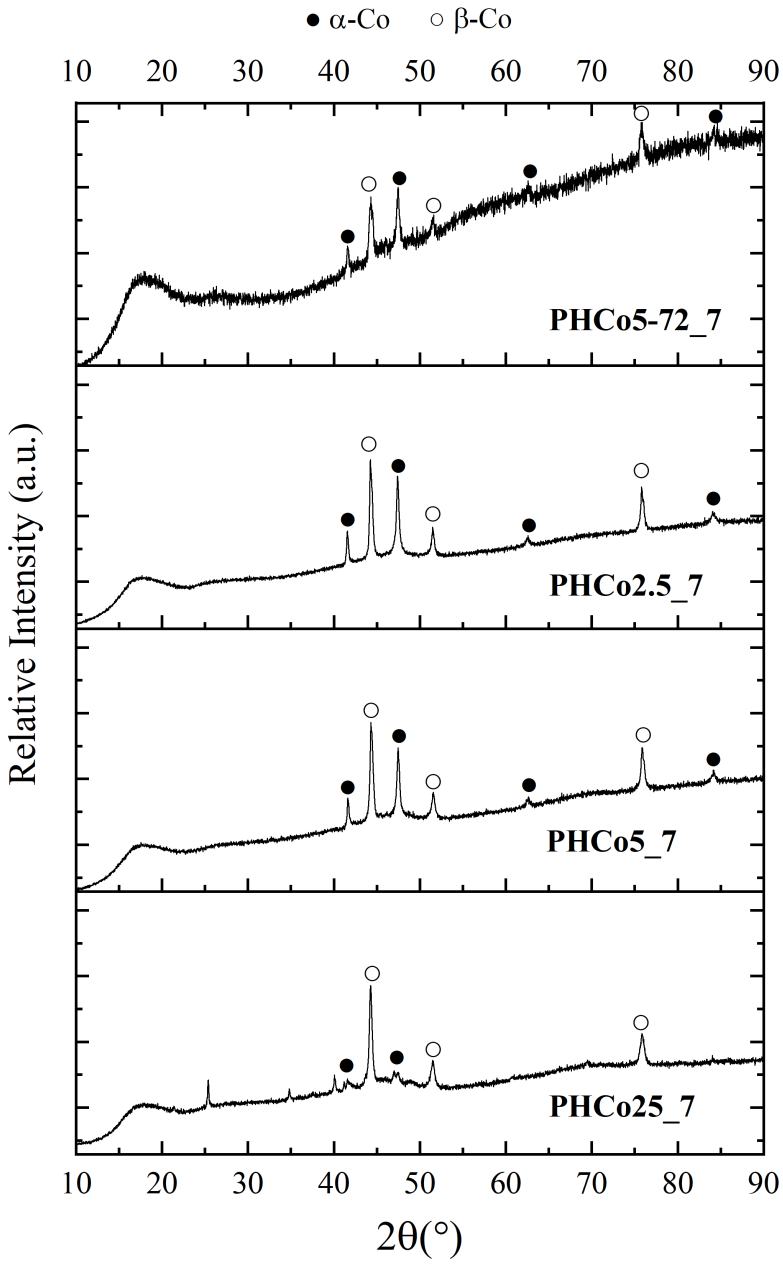

Fig. 4. XRD patterns of the **PHCo25_7**, **PHCo5_7**, **PHCo2.5_7** and **PHCo5-72_7** samples.

The addition of a low Co content in PHPS to form **PHCo25** leads to the growth of a β (fcc)-Co phase after pyrolysis at 700 °C in flowing ammonia (space group Fm-3m,

lattice constant a = 0.35447 nm, ICDD 00-015-0806) as confirmed by the indexation of the peaks at 2θ = 44.5° (111), 51.6° (200) and 75.7° (220) [46] identified in the XRD pattern of **PHCo25_7**. In addition, it can be observed the emergence of two poorly intense XRD peaks at 2θ = 41.9° (100) and 47.6° (101); these positions are related to the diffraction of the α (hcp)-Co phase (space group P63/mmc, lattice constants a = 0.25071 nm, c = 0.408686 nm, ICDD 04-001-3273) [46]. It is well known that at normal conditions, bulk cobalt crystallizes in two phases: hexagonal closed packing (hcp, α) and face-centred cubic (fcc, β) [47]. The striking difference between these two phases is the stacking of atoms, i.e., in β-Co, it is ABCABC while in α-Co, it is ABABAB [48]. Earlier studies on cobalt systems revealed that the synthesis conditions affect the phase formations and lead to either single or mixed phases [49]. In general, it is found that a single exclusive phase formation is probable when low-temperature methods are employed [50], while the combination of phases is probable when high-temperature methods are adopted [46]. In addition, it has been reported [51] that the stability of the phase of cobalt depends on the size of the particle, reduction atmosphere, and temperature. For example, cobalt nanoparticles [49] have been synthesized and, depending on the particle size, either it exists in β-Co (less than 20 nm) or α-Co (above 40 nm) [49]. Both phases are preferred if the particle size is between 20 and 40 nm [49]. Herein, an average crystallite size of 21.17 nm has been calculated using Scherrer's formula for the β-Co phase identified in **PHCo25_7**. Further weak peaks appear at 2θ = 25.4, 34.8, 40.0, 41.0, and 46.9° in a 2θ range in which peaks related to cobalt silicide (CoSi, $CoSi_2$, Co_2Si, …) and/or cobalt silicate phases can be identified [52]. However, given a concise and precise attribution of all the peaks is not easy: peaks at 2θ = 34.8 and 40.0° can be attributed to the (111) and (200) diffraction peaks of the CoSi (ICDD 01-079-8014) [52,53] whereas the peaks at 25.4 and 46.9° can be attributed to the Co_2SiO_4

and Co_2Si phases, respectively [54]. The formation of $CoSi_x$ (x = 1, 2) most probably results from the reaction of $CoCl_2$ with the Si centre of PHPS upon pyrolysis as it occurs during the synthesis of cobalt silicide NPs via microwave-assisted route of $CoCl_2$ and Si powders according to Eq. (1) [54].

$$2CoCl_2 + (2x+1)\ Si \rightarrow 2CoSi_x + SiCl_4 \quad (1)$$

CoSi is a metastable phase having the tendency to further react with Si to form the $CoSi_2$ phase [54].

In addition, $CoCl_2$ reacts with Si to form Co_2Si nanoparticles and $SiCl_4$ according to Eq. (2) [54]:

$$4CoCl_2 + 3Si \rightarrow 2Co_2Si + SiCl_4 \quad (2)$$

Decreasing the atomic Si:Co ratio in the precursor, thereby increasing the Co content in the early stage of the process, tends to vanish the XRD peaks of the secondary cobalt silicide phases, stabilize the β-Co phases in the derived samples and significantly increase the relative XRD peak intensities of the α-Co phase. (102) and (103) XRD peaks of the α-Co phase are even identified in the patterns of **PHCo5_7** and **PHCo2.5_7** at 62.5 and 84.1°, respectively. The α-Co crystallite sizes are quite similar between all samples and range from 24.8 nm (**PHCo5_7**) to 26.1 nm (**PHCo2.5_7**) while the β-Co crystallite sizes range from 21.7 nm (**PHCo25_7**) to 28.0 nm (**PHCo2.5_7**). This agrees with previous predictions [49]. The XRD pattern of the **PHCo5-72_7** sample confirms the signature of α and β-Co phases (crystallite sizes of 25.8 and 24.4 nm).

Then, the evolution of the XRD patterns of **PHCo5-72_7** and **PHCo5_7** after heat-treatment at 800 °C (**PHCo5-72_8** and **PHCo5_8**), 900 °C (**PHCo5-72_9** and **PHCo5_9**) and 1000 °C (**PHCo5-72_10** and **PHCo5_10**) (Fig. 5) has been investigated. Whereas the phase composition and crystallinity of the samples remains quite stable after pyrolysis at

800 °C (while the average crystallite size slightly increases to 25.8 nm for **PHCo5-72_8**), the temperature rise to 900 then 1000 °C induces – as a major fact – the nucleation (900 °C) then the growth (1000 °C) of α (ICDD PDF number: 04-005-5074) and β (ICDD PDF number: 04-033-1160) -Si_3N_4. In addition, XRD peaks related to α-Co gradually disappear while the dicobalt silicide (Co_2Si) phase (ICDD 04-003-2126) is identified through the emergence of some peaks (at 45.2°, 45.9°, 48.7°, 53.7°, 88.1° and 88.8°).

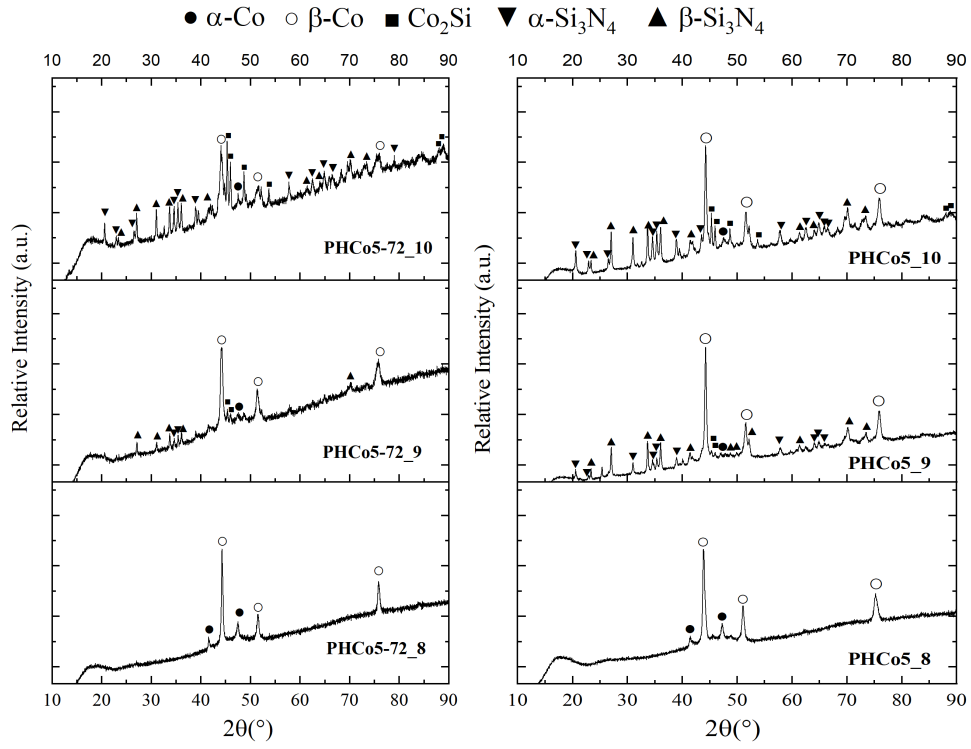

(a) (b)

Fig. 5. XRD evolution of (a) **PHCo5-72_X** and (b) **PHCo5_X** (X = 8, 9 and 10) samples.

The crystallization extend of Si_3N_4 is more pronounced in the **PHCo5-72_X** compared with **PHCo5_X** (X = 9, 10) most probably because the **PHCo5-72** precursor established more Si-N bonds in its structure (higher crosslinking degree) than the **PHCo5** precursor. The growth of crystalline Si_3N_4 significantly affects the measurement of the average crystallize size of the β-Co phase for samples prepared at 900 (**PHCo5-72_9**) and

1000 °C (**PHCo5-72_10**). Then, the effect of Ni on the structure of samples derived from **PHNi5** (i.e., **PHNi5-72_X**; X from 7 to 10 (Fig. 6)) has been investigated.

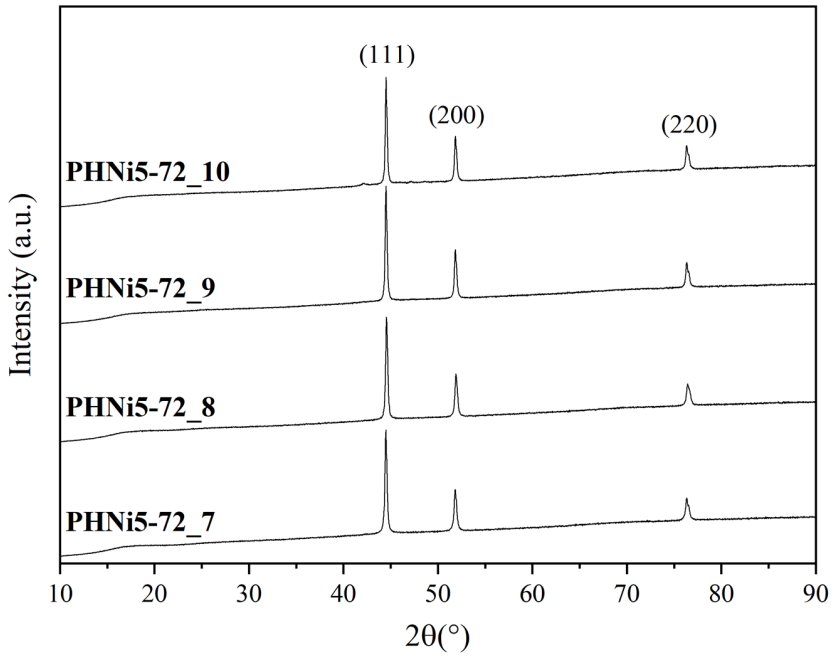

Fig. 6. XRD evolution of **PHNi5-72_X** (X = 7, 8, 9 and 10) samples.

The heat-treatment of **PHNi5** at 700 °C results in the formation of nickel crystals (ICDD 00-004-0850) based on the identification of three characteristic diffraction peaks for pure nickel at 44.5°, 51.8°, and 76.3°. These peaks correspond to the indexed planes (111), (200), and (220) lattice planes of the stable fcc structure of Ni, respectively. This phase composition is characteristic of the whole system evolving from 700 to 1000 °C and only an increase of the average crystallite size is observed; it changes from 42.7 nm (**PHNi5-72_7**) to 56.9 nm (**PHNi5-72_10**) from the most intense peak (111) of the XRD diffraction pattern using the Scherrer formula. Therefore, the Si_3N_4 phase stays amorphous in the explored temperature range. This means that samples prepared from **PHNi5** represent Ni nanoparticles distributed in an amorphous Si_3N_4 matrix. Consequently, Co significantly promotes the crystallization of PHPS-derived Si_3N_4 considering that PHPS-derived Si_3N_4 has been reported to crystallize at around 1200 °C

using ammonia as atmosphere [55]. Thus, following the comment on the higher catalytic effect of Co towards dehydrocoupling than Ni, the fact that the interaction between $CoCl_2$ and PHPS upon heat-treatment is much higher than between $NiCl_2$ and PHPS has been confirmed; the former allowing to establish more Si-N-units in the PHPS network compared to the latter; thereby favouring the conversion (and crystallization) into (of) Si_3N_4 at lower temperature.

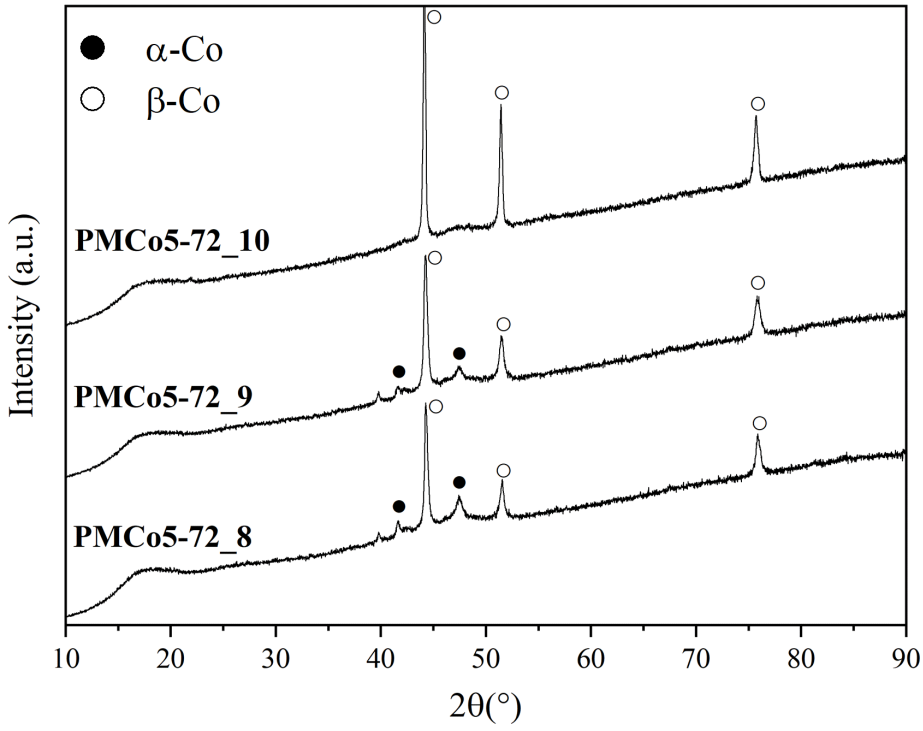

Fig. 7. XRD evolution of **PMCo5-72_X** (X = 8, 9 and 10) samples.

Similar to the structural behaviour of **PHNi5** and in total opposition with **PHCo5-72**, the XRD patterns (Fig. 7) of the PMCo5-72_X samples (X from 7 to 9) display the signature of Co including α- (2θ = 41.6° (100) and 47.4° (101)) and β- (2θ = 44.5° (111), 51.6° (200) and 75.7° (220)) Co phases and CoSi (2θ = 40.0° (200)) whereas the XRD pattern of the **PMCo5-72_10** sample exhibits the unique signature of the β-Co phase. This indicates that Si_3N_4 does not crystallize upon heat-treatment in all PMVMSZ-derived samples allowing the average crystallite sizes of β-Co particles to increase: 26.3

nm for **PMCo5-72_7** and 29.2 nm for **PMCo5-72_8** to be compared to **PHCo5-72**-derived samples. Thus, it is noticeable that PHPS tends to form Si_3N_4 crystals at much lower temperature than PMVMSZ, which can rely on the fact that dehydrocoupling reactions were demonstrated to occur mainly in PHPS-based systems; thus, forming further Si-N bonds which inherently tend to form at lower temperature Si_3N_4 and accelerate its nucleation then growth. In both cases (**PHCo5-72_10** and **PMCo5-72_10**), the XRD peaks attributed to the α-Co phase gradually disappear with the increase of the exposure temperature because of the allotropic phase transformation at an equilibrium temperature *T*0 (at constant pressure) characteristics of a martensitic transformation [52].

To gather further micro- and nanostructural information on the phase formation, identification and distribution, samples have been subjected to a thorough HRTEM analysis that have been coupled with STEM. **PHCo5-72_8** (composed of α- and β-Co phases), **PHCo5-72_10** (composed of α- and β-Co/Si_3N_4 phases), **PMCo5-72_10** (composed of the β-Co phase distributed in an amorphous matrix) and **PHNi5-72_10** (composed of the Ni phase) samples are selected to investigate their micro-/nanostructural features (Fig. 8-11).

The STEM images of **PHCo5-72_8** sample (Fig. 8) demonstrate the localization of particles as imaged in dark (DF, Fig. 8A) and bright (BF, Fig. 8B) field modes. While corresponding dark spots may be found in the same location in the BF images, it appears that the size of the particles can extend over several hundred of nanometers.

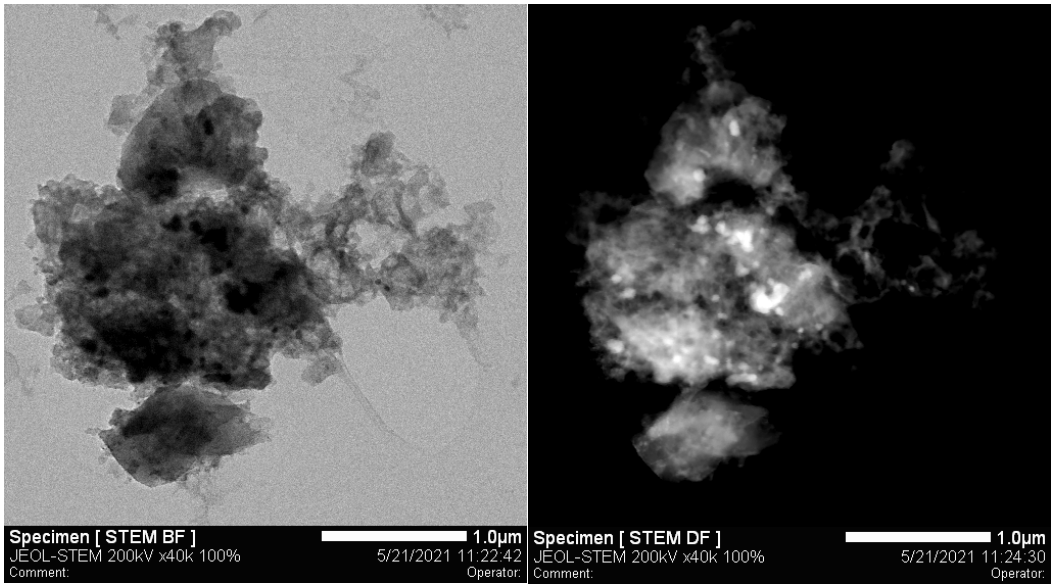

(a) (b)

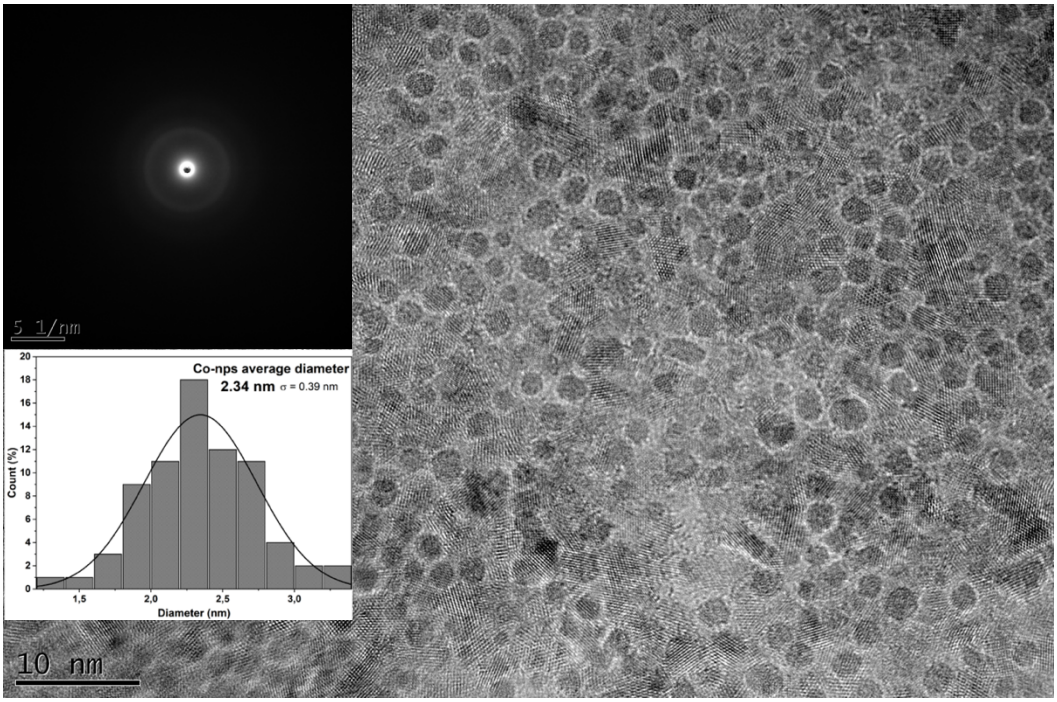

(c)

Fig. 8. STEM images of **PHCo5-72_8** in bright-field (BF) (a) and dark-field (DF) (b) and TEM image of **PHCo5-72_8** (inset: SAED pattern and statistical measurement of particle diameters) (c).

Interestingly, the occurrence of NP clustering or aggregation is limited at the observed scale. Then, HRTEM in an area with the smallest particles (Fig. 8C) has been assessed. It is possible to observe the local distribution of small nuclei with a calculated

average diameter of 2.34 ± 0.39 nm according to the size distribution of nanoparticles (inset of Fig. 8C). These nanoclusters are homogeneously distributed in a featureless matrix typical of amorphous (or poorly crystallized) matrix. The corresponding selected area electron diffraction (SAED) pattern shows a highly diffuse ring whereas a zoom of the TEM image (*See Fig. S2 in Supplementary Material*) allows measuring lattice distances values of around 0.20 nm which could correspond to the (002) and the (111) plane of both hcp-Co and fcc-Co phases. Thus, this provides evidence that the **PHCo5-72_8** sample is composed of a relatively large range of NP size combining α- and β-Co phase with a limited agglomeration. Upon heat-treatment to 1000 °C (**PHCo5-72_10**), STEM images in BF and DF modes confirm the presence of relatively big particles (more than 200 nm) along with smaller particles (Fig. 9A,B). A deeper investigation of the structure of the smallest particles by HRTEM (Fig. 9C) show clear evidence for the growth of the Co NPs. The latter appear as small particles with an average diameter of 7.58 nm (σ = 1.63) as calculated according to the particle size distribution (inset of Fig. 9C). The SAED pattern (inset in Fig. 9C) is composed of distinct spots at 0.217, 0.204, 0.190, 0.180, 0.148, 0.125, 0.115 and 0.107 nm confirming the lattice parameters of fcc and hcp-Co through the attribution of the (100, hcp), (111, fcc)/(002, hcp), (101, hcp), (200, fcc), (102, hcp), (110, hcp)/(220, fcc), and (103, hcp) and (311, fcc) planes. Thus, it indicates the higher degree of crystallinity of the Co phases. Although the indexation of the lattice planes of Si_3N_4 ss not possible in the SAED pattern, we clearly distinguish the presence of Si_3N_4 nanocrystals with a fringe spacing of 0.44 nm in the HRTEM image of the samples (*See Fig. S3 in Supplementary Material*).

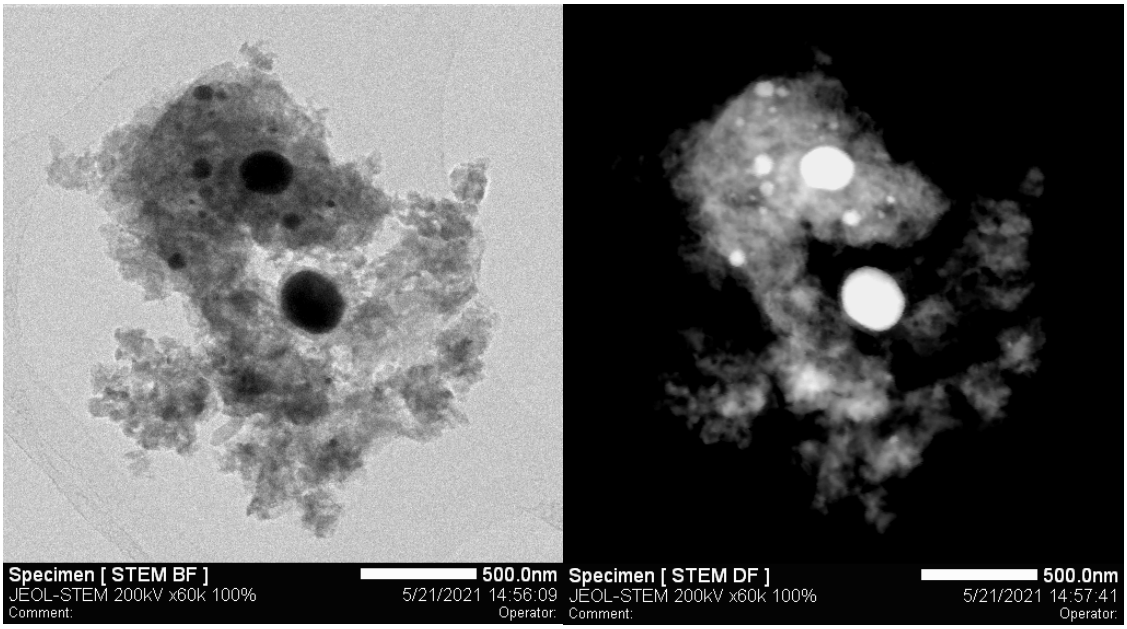

(a) (b)

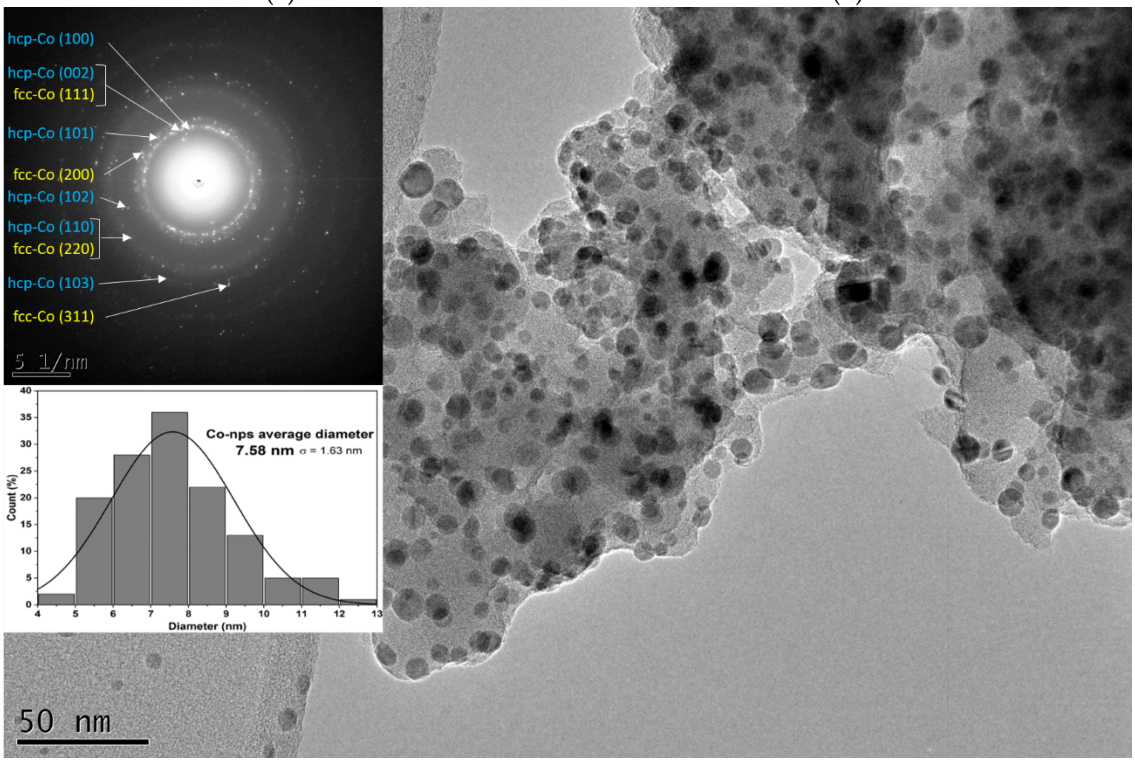

(c)

Fig. 9. STEM images in the BF (a) and DF (b) modes and HRTEM image (Inset: corresponding SAED pattern and statistical measurement of particle diameters) of **PHCo5-72_10**.

The heterogeneity in the Co particle size is confirmed in the STEM images of **PMCo5-72_10** in BF and DF modes (Fig. 10A, B).

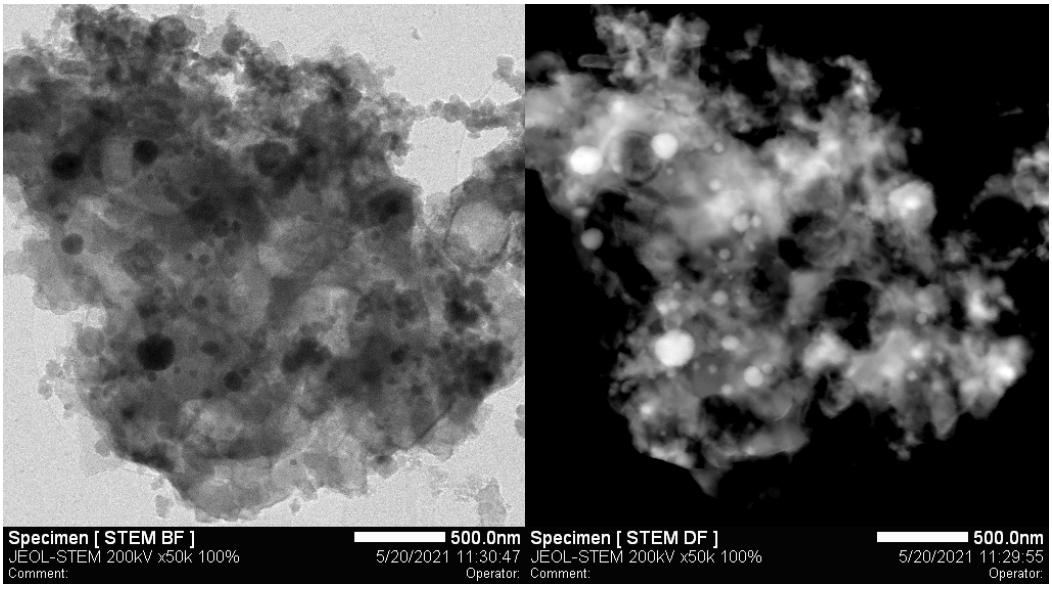

(a) (b)

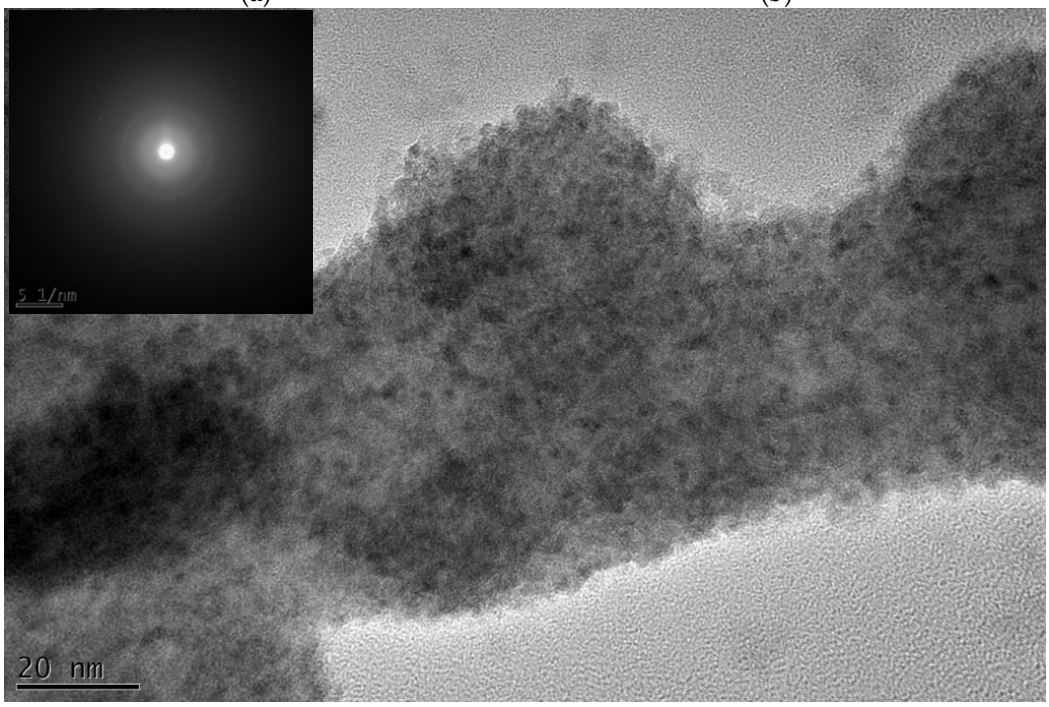

(c)

Fig. 10. STEM images of **PMCo5-72_10** in BF (a) and DF (b) mode and HRTEM image of **PMCo5-72_10** (Inset: corresponding SAED pattern) (c).

However, a strong difference in terms of microstructure definition is shown through HRTEM (Fig. 10C). The TEM investigation demonstrates that the material is less crystallized than its **PHCo5-72_10** counterpart. The diffuse character of the rings composing the SAED pattern as inset in Fig. 10C confirms these observations. The lattice

planes of β-Co are present in the HRTEM image of Fig. 10C as very small nuclei with a fringe spacing of about 0.205 nm embedded in an amorphous matrix.

TEM images of the **PHNi5-72_10** samples (Fig. 11) are consistent with the XRD discussion and confirm the formation of Ni nanoparticles distributed in an amorphous matrix. Interestingly, the particle size is more homogeneous, and the samples is mostly composed of particles with 45 nm in diameter. The associated SAED pattern - composed of spots indicating the high crystallinity of the analyzed phase – confirms the XRD results: the calculation of the d-spacing from the SAED gives values corresponding to the (111), (200), (220), and (311) lattice planes of fcc Ni. The size of the crystals fits with the average crystallite sizes calculated from XRD patterns.

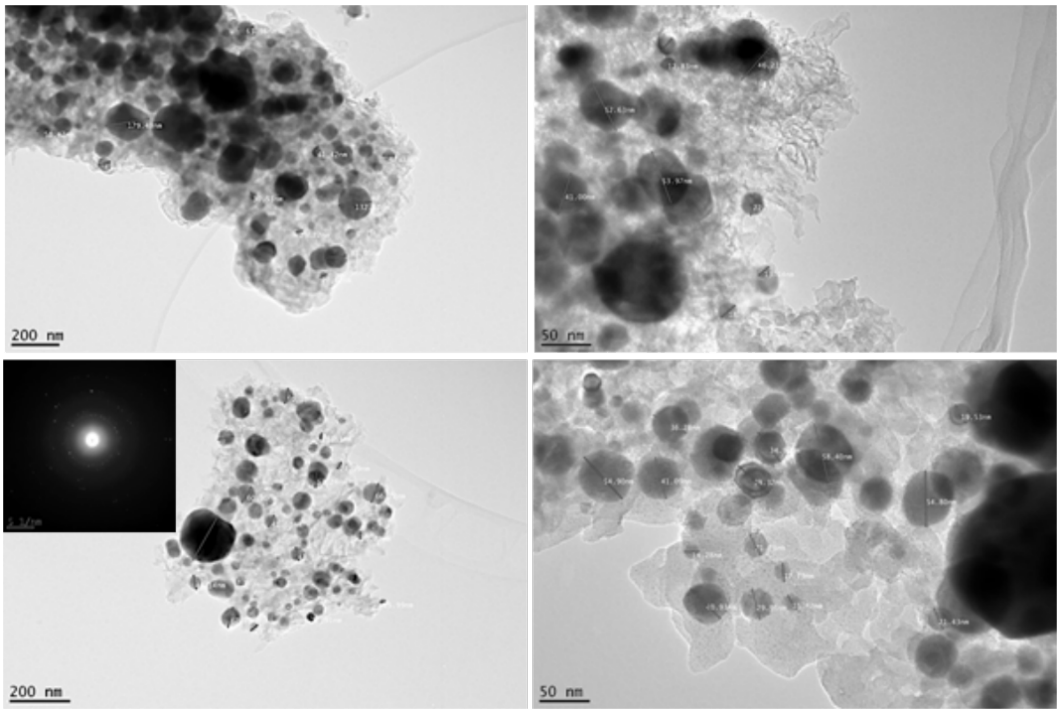

Fig. 11. TEM images of **PHNi5-72_10** (Inset: corresponding SAED pattern).

Because TM NPs in a matrix playing the role of a support have been generated, such materials can be considered as self-supported catalysts for a large range of reactions, as for the catalytic hydrolysis of sodium borohydride. However, the development of the

mesoporosity of the matrix has to be considered to render accessible the metal NPs. As a consequence, the design of mesoporous components is considered in the following section.

3.3 Design of mesoporous monolithic TM/Si_3N_4 (TM = Co, Ni) samples

The strategy to design mesoporous monoliths consists to firstly coat activated carbon monoliths (AC) with the precursors which have been previously characterized to macroscopically shape the monolithic-type structure of the support. Thus, AC is deliberately kept as a support matrix to overcome the problems related to the poor mechanical stability of PDCs with highly developed mesoporosity [56,57]. After solvent extraction, the approach occurs via a two-step pyrolysis under nitrogen (400 °C) to crosslink the precursors surrounding AC support, then under ammonia (800-1000 °C) to form the mesoporous samples which reproduces the monolithic shape of AC samples (Fig. 12). They are labelled with m before the labels previously used. The **mPHCo2.5_8**, **mPHCo5_8**, **mPHCo25_8**, **mPHCo5-72_10**, **mPHNi5-72_10** and **mPMCo5-72_10** samples have been characterized by nitrogen sorption measurements at 77 K (*See Fig. S4 in Supplementary Material*).

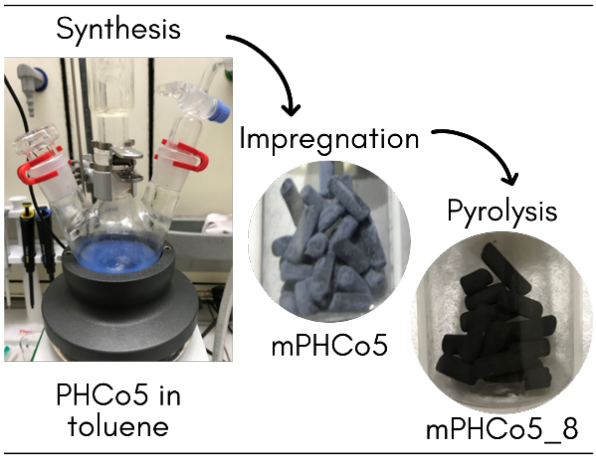

Fig. 12. General process to design micro-/mesoporous TM/Si_3N_4 nanocomposites.

It should be mentioned that the results gained from the **mPHCo5-72_8** samples are close to those of the **mPHCo5_8** sample; thereby they are not reported. The analysis of the nitrogen sorption isotherms by the Brunauer-Emmett-Teller (BET) method reveals that all samples have similar complex isotherms composed of types II and IV [58]. This observation is based on the isotherm profiles as the pressure increases. At pressures P/P_0 lower than 0.45, all the samples present a type II isotherm behaviour, attributed to monolayer-multilayer adsorption, suggesting the presence of microporosity at such relative pressures. With the pressure P/P_0 above 0.45, type IV isotherms are clear, associated to capillary condensation taking place in the mesopores. This is reflected in the distinct hysteresis loops which take place between the adsorption and desorption curves, i.e., the saturation pressures are not equal for condensation and evaporation inside the pores, so that adsorption and desorption isotherms do not coincide.

Considering the IUPAC classification for hysteresis loops, as-prepared monoliths can be classified as type H2 [58] because of a hysteresis commonly found in disordered porous materials or in ordered mesoporous materials with 3D cage-like and interconnected pores [59]. Considering the activated carbon template structure [56,57], investigated samples can be considered as disordered micro-/mesoporous materials bearing interconnected porosity.

Data gained from the analyses of the N_2 adsorption-desorption isotherms such as the BET specific surface area, the pore volume and the modal pore diameter (MPD) are gathered in Table 2. The BET specific surface areas (SSA) are significantly high and the Barrett-Joyner-Halenda (BJH) analysis suggests a narrow pore size distribution except for **mPHCo5-72_10** and **mPMCo5-72_10** most probably due to the higher pyrolysis temperature. Similar total pore volumes are measured while typical t-Plot micropore volumes varied from 0.20 to 0.34 $cm^3.g^{-1}$ for all samples. Thus, these results prove the

reproducibility of the selected impregnation method and do not allow extracting a tendency regarding the effect of the Si:TM ratio, the type of polysilazane and the metal on these parameters whereas there is one report indicating a reduction on the SSA as the amount of cobalt was increased in the produced sample [60].

Table 2

Specific Surface Area (SSA), Pore Volume (PV), t-plot Micropore Volume (MV) and Modal Pore Diameter (MPD) of investigated samples.

Sample	SSA ($m^2.g^{-1}$)	PV ($cm^3.g^{-1}$)	t-plot MV ($cm^3.g^{-1}$)	MPD (nm)
mPHCo2.5_8	859	0.45	0.31	3.95
mPHCo5_8	922	0.5	0.34	3.7
mPHCo25_8	874	0.45	0.32	3.7
mPHCo5-72_10	850	0.5	0.27	5.75
mPMCo5-72_10	756	0.5	0.20	6.3
mPHNi5-72_10	871	0.5	0.23	3.55

Although the pyrolysis temperature tends to slightly reduce the SSA, the large BET specific surface area of the samples is expected to provide selectivity and active sites to the considered sample to be effectively accessed for catalysis. Furthermore, elemental mapping (Figure 13) reveals the uniform distribution of Co and Ni along with silicon, nitrogen and oxygen at the surface of the samples. EDXS spectroscopy indicates the presence of 18 and 21 (**mPHCo5-72_10**, and **mPMCo5-72_10** samples) and 22 (**mPHNi5-72_10**) wt% of Co and Ni, respectively. Thus, the TM content can be

controlled by adjusting the Si/TM ratio in the early stage of the process (*i.e.*, at the polymer level).

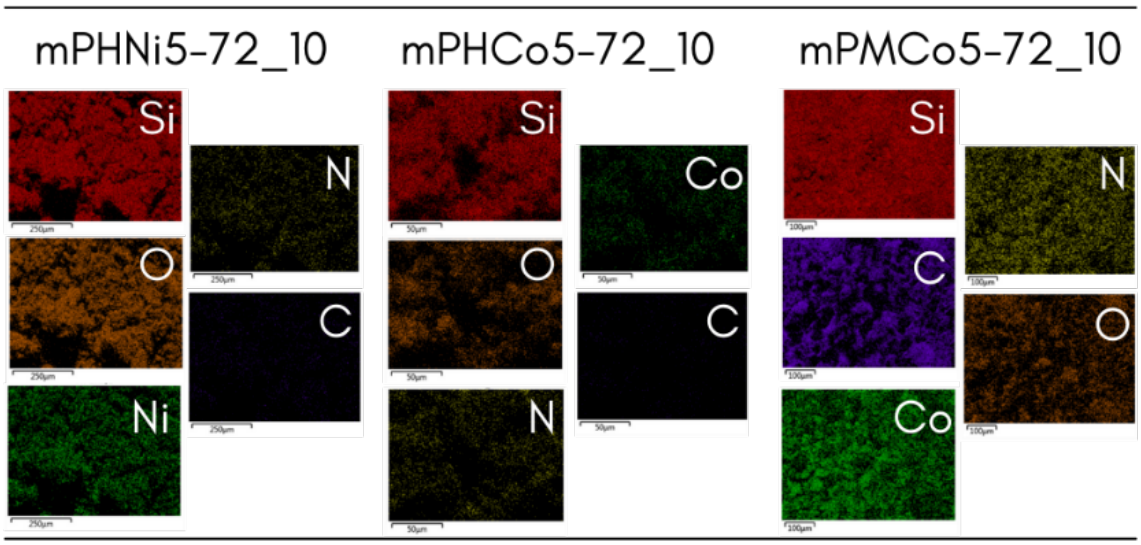

Fig. 13. EDX mapping of **mPHNi5-72_10, mPHCo5-72_10** and **mPMCo5-72_10** samples (SEM x550).

Considering the identification of Co and Ni distributed in a mesoporous Si_3N_4 support, we have checked the potential of these samples for heterogeneous catalysis.

3.4 Catalytic activity of micro-/mesoporous TM/Si_3N_4 (TM = Co, Ni) samples

From the point of view of this work, sodium borohydride ($NaBH_4$; eq. (3)) has been used as a model system to explore the activity of as-produced self-supported catalysts. However, it does not aim at comparing the hydrogen generation rates with previously reported catalysts [61–64]; it provides a rapid overview of the potential of these materials.

$$NaBH_4(aq) + (2 + x)H_2O(l) \xrightarrow{catalyst} NaBO_2.xH_2O(aq) + 4H_2(g) \quad (3)$$

Before the performance of such materials is shown and compared, it is necessary to bring attention to some parameters. The hydrogen generation rate is given as $mL.min^{-1}.g_{catalyst}^{-1}$. This means that the amount of catalyst present in the sample is

inversely proportional to the hydrogen rate. The optimal production (OP) is the method applied to calculate this rate, according to Eq. (3), where $V_{H_2}^{op}$ is the maximum volume of hydrogen generated at an optimal time t^{op} (i.e., slope of the curve) using a known amount of catalyst m_{cat}.

$$\text{OP} = \frac{V_{H_2}^{op}}{m_{cat} x t^{op}} \tag{4}$$

Because, it has been shown that Co powders show higher catalytic activity than Ni powders [65], we have selected the **mPHCo5-72_10** and **mPMCo5-72_10** samples to be used as catalysts for the hydrolysis of $NaBH_4$. Fig. 14 brings hydrogen (H_2) evolution within 180 minutes of hydrolysis.

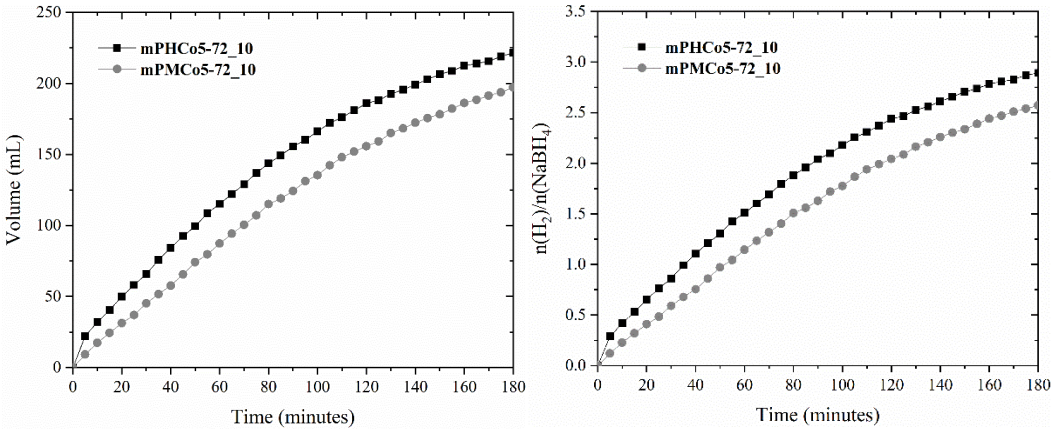

Fig. 14. (a) Volume of H_2 produced during the hydrolysis of $NaBH_4$ and (b) mole of H_2 per mole of $NaBH_4$ using the **mPHCo5-72_10** and **mPMCo5-72_10** samples.

It is interesting to observe that the compounds display a catalytic activity: using the **mPHCo5-72_10** sample, a release of 222 mL of H_2 is measured after 180 minutes of $NaBH_4$ hydrolysis, which is 12.4 % more than with the use of the **mPMCo5-72-10** sample (197 mL). This difference can be related to the crystallization of the matrix and/or the higher SSA of the former. Measured values correspond to a rate of 700 and 540

$mL.min^{-1}.g_{Co}^{-1}$, respectively. Even if conditions are different, the maximum value is 5 times lower than that obtained for support-free Co NPs [66] and PHPS-derived Co/Si_3N_4 compounds are not able to perform the complete release of H_2 from $NaBH_4$ (Fig. 14) after 3 h of reaction (¾ of the reaction is achieved). These facts do not mean that such materials are not appropriate candidates for heterogeneous catalysis. They better mean that they are not suited for the hydrolysis of $NaBH_4$ most probably because of the presence of micropores in the matrix which hinder diffusion of $NaBH_4$ towards Co NPs. Hence, by considering these hypotheses and the fact that these materials display strong nanoparticle-matrix interaction with a limited active site aggregation, templates leading to fully mesoporous TM/Si_3N_4 compounds would be best suitable.

4. Conclusions

As a conclusion, ceramics made of silicon (Si), carbon (C), oxygen (O) and nitrogen (N) elements, surrounding cobalt (Co) or nickel (Ni) nanoparticles by coordination of polysilazanes with Co and Ni chlorides have been prepared. It is shown that Co displays a higher catalytic effect on polysilazanes towards dehydrocoupling than Ni which is demonstrated to affect – in addition to the polysilazane nature and the Si:transition metal ratio - the crystallization behavior of the derived nanocomposites. The latter are made of fcc- and hcp-Co or fcc-Ni particles immobilized in a highly micro/mesoporous PDC matrix via a single-step pyrolysis process at temperatures from 700 to 1000 °C under flowing argon. The development of the SSA and the micro-/mesoporosity of the matrix allowed exploiting the catalytic activity of the samples. Although the complete release of H_2 from $NaBH_4$ was hindered by the presence of microporosity, this study establishes an opportunity to the development of future highly durable self-supported catalysts synthesized using a simple method and tailor-made templates.

Appendix A. Supplementary data

Supplementary material to this article can be found online at https://doi.org/xx.xxxx/j.micromeso. Fig. S1. FTIR spectra of PHPS and **PHNi5-72** (a) PMVMSZ and **PMCo5-72** (b).; Fig. S2. Zoom of Fig. 8 to reach the lattice distance in isolated particles composing the **PHCo5-72_8** sample. Fig. S3. (a) TEM image of **PHCo5-72_10** (Inset: corresponding SAED pattern and statistical measurement of particle diameters) and (b) HRTEM image showing Si_3N_4 crystallites. Fig. S4. N_2 adsorption-desorption isotherms of **mPHCo2.5_8**, **mPHCo5_8**, **mPHCo25_8**, **mPHCo5-72_10**, **mPMCo5-72_10** and **mPHNi5-72_10** samples**.**

CRediT authorship contribution statement

M. Mallmann: Conceptualization, Methodology, Validation, Formal analysis, Investigation, Data curation, Writing - original draft preparation, Writing - review and editing, Visualization. **R. Nishihora:** Formal analysis, Data curation. **E. Acosta:** Formal analysis, Data curation. **P. Carles:** Formal analysis. **N. Asakuma:** Investigation. **S. Tada:** Investigation. **Y. Iwamoto:** Writing: review and editing, Project administration, Funding acquisition. **U. Demirci:** Formal analysis, Writing: review and editing. **R. Machado:** Project administration, Funding acquisition. **S. Bernard:** Conceptualization, Methodology, Resources, Writing - original draft, Writing - review and editing, Visualization, Supervision, Project administration, Funding acquisition.

Declaration of competing interest

The authors declare that they have no known competing financial interests or personal relationships that could have appeared to influence the work reported in this paper.

Funding

This research was funded by Campus France and CAPES through the COFECUB project N°Ph-C 956/19, by CNPq and by CNRS via the International Research Project (IRP, SB and Prof. Y. Iwamoto (YI)) 'Ceramics materials for societal challenges'.

Acknowledgments

Dr. Samuel Bernard and Prof. Ricardo Machado acknowledge the CNPq for providing financial support for the PhD thesis of Maira Mallmann and Campus France and CAPES through the COFECUB project N°Ph-C 956/19 entitled Design of monolithic polymer-derived ceramics nanocomposites with tuned micro-/mesoporosity for energy-related fields for financially support the postdoc fellowship to Dr. Rafael Kenji Nishihora. Dr. Samuel Bernard and Prof. Yuji Iwamoto would like to thank CNRS who financially supported present work via the International Research Project (IRP) 'Ceramics materials for societal challenges'. The authors would like to thank the LCME-UFSC for technical support during electron microscopy work.

References

[1] M.B. Tahir, M. Rafique, M.S. Rafique, M. Sagir, M. Maraj, A. Jabeen, S. Zahid, A. Batool, Photocatalytic nanomaterials for hydrogen evolution from water splitting, Nanotechnology and Photocatalysis for Environmental Applications. (2020) 139–158. https://doi.org/10.1016/B978-0-12-821192-2.00009-7.

[2] Y. Sun, S. Polani, F. Luo, S. Ott, P. Strasser, F. Dionigi, Advancements in cathode catalyst and cathode layer design for proton exchange membrane fuel

cells, Nature Communications 2021 12:1. 12 (2021) 1–14. https://doi.org/10.1038/s41467-021-25911-x.

[3] J.E. Lee, Y.S. Ok, D.C.W. Tsang, J.H. Song, S.C. Jung, Y.K. Park, Recent advances in volatile organic compounds abatement by catalysis and catalytic hybrid processes: A critical review, Science of The Total Environment. 719 (2020) 137405. https://doi.org/10.1016/J.SCITOTENV.2020.137405.

[4] J. Winarta, A. Yung, B. Mu, Hydrogen and methane storage in nanoporous materials, Nanoporous Materials for Molecule Separation and Conversion. (2020) 327–350. https://doi.org/10.1016/B978-0-12-818487-5.00010-8.

[5] D. Gielen, F. Boshell, D. Saygin, Climate and energy challenges for materials science, Nature Materials 2016 15:2. 15 (2016) 117–120. https://doi.org/10.1038/nmat4545.

[6] C. Wang, C. Li, J. Liu, C. Guo, Engineering transition metal-based nanomaterials for high-performance electrocatalysis, Materials Reports: Energy. 1 (2021) 100006. https://doi.org/10.1016/J.MATRE.2021.01.001.

[7] A. Cid, J. Simal-Gandara, Synthesis, Characterization, and Potential Applications of Transition Metal Nanoparticles, Journal of Inorganic and Organometallic Polymers and Materials 2019 30:4. 30 (2019) 1011–1032. https://doi.org/10.1007/S10904-019-01331-9.

[8] Q.-L. Zhou, Q.-L. Zhou, Transition-Metal Catalysis and Organocatalysis: Where Can Progress Be Expected?, Angewandte Chemie International Edition. 55 (2016) 5352–5353. https://doi.org/10.1002/ANIE.201509164.

[9] A. Lale, A. Wasan, R. Kumar, P. Miele, U.B. Demirci, S. Bernard, Organosilicon polymer-derived mesoporous 3D silicon carbide, carbonitride and nitride structures as platinum supports for hydrogen generation by hydrolysis of sodium

borohydride, Int J Hydrogen Energy. 41 (2016) 15477–15488. https://doi.org/10.1016/J.IJHYDENE.2016.06.186.

[10] O. Santoliquido, G. Bianchi, P. Dimopoulos Eggenschwiler, A. Ortona, Additive manufacturing of periodic ceramic substrates for automotive catalyst supports, Int J Appl Ceram Technol. 14 (2017) 1164–1173. https://doi.org/10.1111/IJAC.12745.

[11] D. Xu, H. Lv, B. Liu, Encapsulation of metal nanoparticle catalysts within mesoporous zeolites and their enhanced catalytic performances: A review, Front Chem. 6 (2018) 550. https://doi.org/10.3389/FCHEM.2018.00550/BIBTEX.

[12] M. Zaheer, J. Hermannsdörfer, W.P. Kretschmer, G. Motz, R. Kempe, Robust Heterogeneous Nickel Catalysts with Tailored Porosity for the Selective Hydrogenolysis of Aryl Ethers, ChemCatChem. 6 (2014) 91–95. https://doi.org/10.1002/CCTC.201300763.

[13] D. Schumacher, M. Wilhelm, K. Rezwan, Porous SiOC monoliths with catalytic activity by in situ formation of Ni nanoparticles in solution-based freeze casting, Journal of the American Ceramic Society. 103 (2020) 2991–3001. https://doi.org/10.1111/JACE.16988.

[14] M. Seifollahi Bazarjani, H.J. Kleebe, M.M. Müller, C. Fasel, M. Baghaie Yazdi, A. Gurlo, R. Riedel, Nanoporous silicon oxycarbonitride ceramics derived from polysilazanes in situ modified with nickel nanoparticles, Chemistry of Materials. 23 (2011) 4112–4123. https://doi.org/10.1021/CM200589N/SUPPL_FILE/CM200589N_SI_001.PDF.

[15] D. Forberg, T. Schwob, R. Kempe, Catalytic condensation for the formation of polycyclic heteroaromatic compounds, Nature Communications 2018 9:1. 9 (2018) 1–7. https://doi.org/10.1038/s41467-018-04143-6.

[16] D. Forberg, T. Schwob, M. Zaheer, M. Friedrich, N. Miyajima, R. Kempe, Single-catalyst high-weight% hydrogen storage in an N-heterocycle synthesized from lignin hydrogenolysis products and ammonia, Nature Communications 2016 7:1. 7 (2016) 1–6. https://doi.org/10.1038/ncomms13201.

[17] G. Glatz, T. Schmalz, T. Kraus, F. Haarmann, G. Motz, R. Kempe, Copper-Containing SiCN Precursor Ceramics (Cu@SiCN) as Selective Hydrocarbon Oxidation Catalysts Using Air as an Oxidant, Chemistry – A European Journal. 16 (2010) 4231–4238. https://doi.org/10.1002/CHEM.200902836.

[18] M. Zaheer, T. Schmalz, G. Motz, R. Kempe, Polymer derived non-oxide ceramics modified with late transition metals, Chem Soc Rev. 41 (2012) 5102–5116. https://doi.org/10.1039/C2CS15326B.

[19] D. Forberg, J. Obenauf, M. Friedrich, S.M. Hühne, W. Mader, G. Motz, R. Kempe, The synthesis of pyrroles via acceptorless dehydrogenative condensation of secondary alcohols and 1,2-amino alcohols mediated by a robust and reusable catalyst based on nanometer-sized iridium particles, Catal Sci Technol. 4 (2014) 4188–4192. https://doi.org/10.1039/C4CY01018C.

[20] G. Hahn, J.K. Ewert, C. Denner, D. Tilgner, R. Kempe, A Reusable Mesoporous Nickel Nanocomposite Catalyst for the Selective Hydrogenation of Nitroarenes in the Presence of Sensitive Functional Groups, ChemCatChem. 8 (2016) 2461–2465. https://doi.org/10.1002/CCTC.201600391.

[21] M. Kamperman, A. Burns, R. Weissgraeber, N. van Vegten, S.C. Warren, S.M. Gruner, A. Baiker, U. Wiesner, Integrating structure control over multiple length scales in porous high temperature ceramics with functional platinum nanoparticles, Nano Lett. 9 (2009) 2756–2762. https://doi.org/10.1021/NL901293P.

[22] T. Schwob, R. Kempe, A Reusable Co Catalyst for the Selective Hydrogenation of Functionalized Nitroarenes and the Direct Synthesis of Imines and Benzimidazoles from Nitroarenes and Aldehydes, Angewandte Chemie International Edition. 55 (2016) 15175–15179. https://doi.org/10.1002/ANIE.201608321.

[23] C. Bäumler, R. Kempe, The Direct Synthesis of Imines, Benzimidazoles and Quinoxalines from Nitroarenes and Carbonyl Compounds by Selective Nitroarene Hydrogenation Employing a Reusable Iron Catalyst, Chemistry – A European Journal. 24 (2018) 8989–8993. https://doi.org/10.1002/CHEM.201801525.

[24] N. Yang, K. Lu, Effects of transition metals on the evolution of polymer-derived SiOC ceramics, Carbon N Y. 171 (2021). https://doi.org/10.1016/j.carbon.2020.08.072.

[25] Y. Zhao, L. Guo, Q. Ma, Influence of Ni on the structural evolution of polymer-derived SiOC ceramics, Journal of Materials Research and Technology. 20 (2022). https://doi.org/10.1016/j.jmrt.2022.09.004.

[26] T. Canuto De Almeida E Silva, M. Mooste, E. Kibena-Põldsepp, L. Matisen, M. Merisalu, M. Kook, V. Sammelselg, K. Tammeveski, M. Wilhelm, K. Rezwan, Polymer-derived Co/Ni-SiOC(N) ceramic electrocatalysts for oxygen reduction reaction in fuel cells, Catal Sci Technol. 9 (2019). https://doi.org/10.1039/c8cy02207k.

[27] Y. Han, X. Yue, Y. Jin, X. Huang, P.K. Shen, Hydrogen evolution reaction in acidic media on single-crystalline titanium nitride nanowires as an efficient non-noble metal electrocatalyst, J Mater Chem A Mater. 4 (2016) 3673–3677. https://doi.org/10.1039/C5TA09976E.

[28] M.S. Balogun, W. Qiu, W. Wang, P. Fang, X. Lu, Y. Tong, Recent advances in metal nitrides as high-performance electrode materials for energy storage devices, J Mater Chem A Mater. 3 (2014) 1364–1387. https://doi.org/10.1039/C4TA05565A.

[29] W. Yang, S. Rehman, X. Chu, Y. Hou, S. Gao, Transition Metal (Fe, Co and Ni) Carbide and Nitride Nanomaterials: Structure, Chemical Synthesis and Applications, ChemNanoMat. 1 (2015) 376–398. https://doi.org/10.1002/CNMA.201500073.

[30] M.S. Balogun, Y. Huang, W. Qiu, H. Yang, H. Ji, Y. Tong, Updates on the development of nanostructured transition metal nitrides for electrochemical energy storage and water splitting, Materials Today. 20 (2017) 425–451. https://doi.org/10.1016/J.MATTOD.2017.03.019.

[31] J.S.J. Hargreaves, Heterogeneous catalysis with metal nitrides, Coord Chem Rev. 257 (2013) 2015–2031. https://doi.org/10.1016/J.CCR.2012.10.005.

[32] S. Dong, X. Chen, X. Zhang, G. Cui, Nanostructured transition metal nitrides for energy storage and fuel cells, Coord Chem Rev. 257 (2013) 1946–1956. https://doi.org/10.1016/J.CCR.2012.12.012.

[33] S. Tada, M.D. Mallmann, H. Takagi, J. Iihama, N. Asakuma, T. Asaka, Y. Daiko, S. Honda, R.K. Nishihora, R.A.F. Machado, S. Bernard, Y. Iwamoto, Low temperature in situ formation of cobalt in silicon nitride toward functional nitride nanocomposites, Chemical Communications. 57 (2021) 2057–2060. https://doi.org/10.1039/D0CC07366K.

[34] N. Asakuma, S. Tada, E. Kawaguchi, M. Terashima, S. Honda, R.K. Nishihora, P. Carles, S. Bernard, Y. Iwamoto, Mechanistic Investigation of the Formation of Nickel Nanocrystallites Embedded in Amorphous Silicon Nitride

Nanocomposites, Nanomaterials. 12 (2022). https://doi.org/10.3390/NANO12101644/S1.

[35] C. Salameh, A. Bruma, S. Malo, U.B. Demirci, P. Miele, S. Bernard, Monodisperse platinum nanoparticles supported on highly ordered mesoporous silicon nitride nanoblocks: superior catalytic activity for hydrogen generation from sodium borohydride, RSC Adv. 5 (2015) 58943–58951. https://doi.org/10.1039/C5RA05901A.

[36] O. Majoulet, C. Salameh, M.E. Schuster, U.B. Demirci, Y. Sugahara, S. Bernard, P. Miele, Preparation, characterization, and surface modification of periodic mesoporous silicon-aluminum-carbon-nitrogen frameworks, Chemistry of Materials. 25 (2013) 3957–3970. https://doi.org/10.1021/CM401605A/SUPPL_FILE/CM401605A_SI_001.PDF.

[37] M. Zaheer, J. Hermannsdörfer, W.P. Kretschmer, G. Motz, R. Kempe, Robust Heterogeneous Nickel Catalysts with Tailored Porosity for the Selective Hydrogenolysis of Aryl Ethers, ChemCatChem. 6 (2014) 91–95. https://doi.org/10.1002/cctc.201300763.

[38] T.J. Clark, K. Lee, I. Manners, Transition-Metal-Catalyzed Dehydrocoupling: A Convenient Route to Bonds between Main-Group Elements, Chemistry – A European Journal. 12 (2006) 8634–8648. https://doi.org/10.1002/CHEM.200600981.

[39] R. Giri, N. Maugel, J.J. Li, D.H. Wang, S.P. Breazzano, L.B. Saunders, J.Q. Yu, Palladium-catalyzed methylation and arylation of sp2 and sp 3 C-H bonds in simple carboxylic acids, J Am Chem Soc. 129 (2007) 3510–3511. https://doi.org/10.1021/JA0701614/SUPPL_FILE/JA0701614SI20070208_061114.PDF.

[40] O. Daugulis, H.Q. Do, D. Shabashov, Palladium- and copper-catalyzed arylation of carbon-hydrogen bonds, Acc Chem Res. 42 (2009) 1074–1086. https://doi.org/10.1021/AR9000058/ASSET/IMAGES/MEDIUM/AR-2009-000058_0001.GIF.

[41] R. Jazzar, J. Hitce, A. Renaudat, J. Sofack-Kreutzer, O. Baudoin, Functionalization of Organic Molecules by Transition-Metal-Catalyzed C(sp3) H Activation, Chemistry – A European Journal. 16 (2010) 2654–2672. https://doi.org/10.1002/CHEM.200902374.

[42] V.C. Gibson, S.K. Spitzmesser, Advances in non-metallocene olefin polymerization catalysis, Chem Rev. 103 (2003) 283–315. https://doi.org/10.1021/CR980461R/ASSET/CR980461R.FP.PNG_V03.

[43] S.C.K. Yive, R.J.P. Corriu, D. Leclercq, P.H. Mutin, A. Vioux, Silicon Carbonitride from Polymeric Precursors: Thermal Cross-Linking and Pyrolysis of Oligosilazane Model Compounds, Chemistry of Materials. 4 (1992) 141–146. https://doi.org/10.1021/CM00019A029/ASSET/CM00019A029.FP.PNG_V03.

[44] M. Balestrat, A. Lale, A.V.A. Bezerra, V. Proust, E.W. Awin, R.A.F. Machado, P. Carles, R. Kumar, C. Gervais, S. Bernard, In-Situ Synthesis and Characterization of Nanocomposites in the Si-Ti-N and Si-Ti-C Systems, Molecules 2020, Vol. 25, Page 5236. 25 (2020) 5236. https://doi.org/10.3390/MOLECULES25225236.

[45] E. Bernardo, L. Fiocco, G. Parcianello, E. Storti, P. Colombo, Advanced ceramics from preceramic polymers modified at the nano-scale: A review, Materials. 7 (2014). https://doi.org/10.3390/ma7031927.

[46] M. Manjunatha, G.S. Reddy, K.J. Mallikarjunaiah, R. Damle, K.P. Ramesh, Determination of Phase Composition of Cobalt Nanoparticles Using 59Co

Internal Field Nuclear Magnetic Resonance, J Supercond Nov Magn. 32 (2019) 3201–3209. https://doi.org/10.1007/S10948-019-5083-7/TABLES/2.

[47] Y.T. Jeon, J.Y. Moon, G.H. Lee, J. Park, Y. Chang, Comparison of the Magnetic Properties of Metastable Hexagonal Close-Packed Ni Nanoparticles with Those of the Stable Face-Centered Cubic Ni Nanoparticles, Journal of Physical Chemistry B. 110 (2005) 1187–1191. https://doi.org/10.1021/JP054608B.

[48] S. Kajiwara, S. Ohno, K. Honma, M. Uda, A new crystal structure of pure cobalt formed in ultrafine particles, Https://Doi.Org/10.1080/09500838708203752. 55 (2006) 215–219. https://doi.org/10.1080/09500838708203752.

[49] O. Kitakami, H. Sato, Y. Shimada, F. Sato, M. Tanaka, Size effect on the crystal phase of cobalt fine particles, Phys Rev B. 56 (1997) 13849. https://doi.org/10.1103/PhysRevB.56.13849.

[50] D.P. Dinega, M. Bawendi, A Solution-Phase Chemical Approach to a New Crystal Structure of Cobalt., Undefined. (1999). https://doi.org/10.1002/(SICI)1521-3773(19990614)38:12.

[51] V.A. de La Peña O'Shea, P.R. de la Piscina, N. Homs, G. Aromí, J.L.G. Fierro, Development of hexagonal closed-packed cobalt nanoparticles stable at high temperature, Chemistry of Materials. 21 (2009) 5637–5643. https://doi.org/10.1021/CM900845H/SUPPL_FILE/CM900845H_SI_001.PDF.

[52] M. Longhin, R. Viennois, D. Ravot, J.J. Robin, P. Papet, Nanostructuration of CoSi by mechanical milling and mechanical alloying, Solid State Sci. 38 (2014) 129–137. https://doi.org/10.1016/J.SOLIDSTATESCIENCES.2014.10.011.

[53] D. Potoczna-Petru, L. Kępiński, L. Krajczyk, Interaction of Co nanoparticles with SiO 2 : Silicide formation, Reaction Kinetics and Catalysis Letters. 97 (2009) 321–327. https://doi.org/10.1007/S11144-009-0033-1/FIGURES/4.

[54] L. Zhang, X. Chen, S. Jin, J. Guan, C.T. Williams, Z. Peng, C. Liang, Rapid microwaves synthesis of CoSix/CNTs as novel catalytic materials for hydrogenation of phthalic anhydride, J Solid State Chem. 217 (2014) 105–112. https://doi.org/10.1016/J.JSSC.2014.05.021.

[55] A. Lale, V. Proust, M.C. Bechelany, A. Viard, S. Malo, S. Bernard, A comprehensive study on the influence of the polyorganosilazane chemistry and material shape on the high temperature behavior of titanium nitride/silicon nitride nanocomposites, J Eur Ceram Soc. 37 (2017) 5167–5175. https://doi.org/10.1016/J.JEURCERAMSOC.2017.04.001.

[56] C. Salameh, G. Moussa, A. Bruma, G. Fantozzi, S. Malo, P. Miele, U.B. Demirci, S. Bernard, Robust 3D Boron Nitride Nanoscaffolds for Remarkable Hydrogen Storage Capacity from Ammonia Borane, Energy Technology. 6 (2018) 570–577. https://doi.org/10.1002/ENTE.201700618.

[57] A. Lale, M.D. Mallmann, S. Tada, A. Bruma, S. Özkar, R. Kumar, M. Haneda, R.A. Francisco Machado, Y. Iwamoto, U.B. Demirci, S. Bernard, Highly active, robust and reusable micro-/mesoporous TiN/Si3N4 nanocomposite-based catalysts for clean energy: Understanding the key role of TiN nanoclusters and amorphous Si3N4 matrix in the performance of the catalyst system, Appl Catal B. 272 (2020) 118975. https://doi.org/10.1016/J.APCATB.2020.118975.

[58] M. Thommes, K. Kaneko, A. V. Neimark, J.P. Olivier, F. Rodriguez-Reinoso, J. Rouquerol, K.S.W. Sing, Physisorption of gases, with special reference to the evaluation of surface area and pore size distribution (IUPAC Technical Report), Pure and Applied Chemistry. 87 (2015) 1051–1069. https://doi.org/10.1515/PAC-2014-1117/MACHINEREADABLECITATION/RIS.

[59] G. Mason, The effect of pore space connectivity on the hysteresis of capillary condensation in adsorption—desorption isotherms, J Colloid Interface Sci. 88 (1982) 36–46. https://doi.org/10.1016/0021-9797(82)90153-9.

[60] Z. Li, A.A. Haidry, B. Gao, T. Wang, Z.J. Yao, The effect of Co-doping on the humidity sensing properties of ordered mesoporous TiO2, Appl Surf Sci. 412 (2017) 638–647. https://doi.org/10.1016/J.APSUSC.2017.03.156.

[61] P. Brack, S.E. Dann, K.G. Upul Wijayantha, Heterogeneous and homogenous catalysts for hydrogen generation by hydrolysis of aqueous sodium borohydride (NaBH4) solutions, Energy Sci Eng. 3 (2015) 174–188. https://doi.org/10.1002/ESE3.67.

[62] A. Uzundurukan, Y. Devrim, Hydrogen generation from sodium borohydride hydrolysis by multi-walled carbon nanotube supported platinum catalyst: A kinetic study, Int J Hydrogen Energy. 44 (2019) 17586–17594. https://doi.org/10.1016/J.IJHYDENE.2019.04.188.

[63] J. Guo, B. Wang, D. Yang, Z. Wan, P. Yan, J. Tian, T.T. Isimjan, X. Yang, Rugae-like Ni2P-CoP nanoarrays as a bi-functional catalyst for hydrogen generation: NaBH4 hydrolysis and water reduction, Appl Catal B. 265 (2020) 118584. https://doi.org/10.1016/J.APCATB.2019.118584.

[64] H. Jadhav, A.K. Singh, N. Patel, R. Fernandes, S. Gupta, D.C. Kothari, A. Miotello, S. Sinha, Pulsed laser deposition of nanostructured Co-B-O thin films as efficient catalyst for hydrogen production, Appl Surf Sci. 387 (2016) 358–365. https://doi.org/10.1016/J.APSUSC.2016.06.118.

[65] B.H. Liu, Z.P. Li, S. Suda, Nickel- and cobalt-based catalysts for hydrogen generation by hydrolysis of borohydride, J Alloys Compd. 415 (2006) 288–293. https://doi.org/10.1016/J.JALLCOM.2005.08.019.

[66] Y. Bu, J. Liu, H. Chu, S. Wei, Q. Yin, L. Kang, X. Luo, L. Sun, F. Xu, P. Huang, F. Rosei, A.A. Pimerzin, H.J. Seifert, Y. Du, J. Wang, Catalytic hydrogen evolution of nabh4 hydrolysis by cobalt nanoparticles supported on bagasse-derived porous carbon, Nanomaterials. 11 (2021). https://doi.org/10.3390/nano11123259.